Late Pleistocene slip rate of the central Haiyuan fault constrained from OSL, 14C, and cosmogenic isotope dating and high-resolution topography

Yanxiu Shao, Jing Liu-Zeng, Jérôme van Der Woerd, Yann Klinger, Michael Oskin, Jinyu Zhang, Peng Wang, Pengtao Wang, Wei Wang, Wenqian Yao

Late Pleistocene slip rate of the central Haiyuan fault constrained from OSL, ^{14}C, and cosmogenic isotope dating and high resolution topography

Yanxiu Shao[1,2,3*], Jing Liu-Zeng[1], Jérôme Van der Woerd[4*], Yann Klinger[2], Michael E. Oskin[5], Jinyu Zhang[6], Peng Wang[6], Pengtao Wang[3], Wei Wang[6], Wenqian Yao[6]

[1]*Institute of Surface-Earth System Science, Tianjin University, Tianjin 300072, China*

[2]*Université de Paris, Institut de Physique du Globe de Paris, CNRS, F-75005 Paris, France*

[3]*Lanzhou Institute of Seismology, China Earthquake Administration, Lanzhou, 730000 China*

[4]*Institut de Physique du Globe de Strasbourg UMR 7516 CNRS Université de Strasbourg, 5 rue René Descartes, 67084 Strasbourg Cedex, France*

[5]*Department of Earth and Planetary Sciences, University of California, Davis, California 95616, USA*

[6]*Institute of Geology, China Earthquake Administration, Beijing, 100029 China*

Y. SHAO: shaoyx@geoidea.org

J. Van der Woerd: jerome.vanderwoerd@unistra.fr

ABSTRACT

To better constrain the long-term millennial slip-rate of the Haiyuan fault in its central part, we revisit the site of Daqing (or Sangedun at 102.7°E in Gaudemer et al., 1995). We used terrestrial LiDAR to build a high-resolution DEM and Uncrewed Aerial Vehicle to build an aerial photomosaic with ~0.1 m resolution to survey the offset terraces, their geomorphology and the fault trace. We refine the geomorphological interpretation of the site, measure terrace riser offsets and determine their relation to terrace formation. The well-constrained age of the highest terrace T3 at 13.7 ± 1.5 ka determined from the combination of surface and sub-surface OSL, ^{14}C, and terrestrial in situ ^{10}Be cosmogenic radionuclide (CRN) dating, associated with an offset of 88 m, yields a late Pleistocene minimum slip-rate of 6.5 ± 1 mm/yr. The less well constrained offset (<72 ± 3 m) and age (>9.3 ± 0.6 ka) of terrace T2 yield a maximum slip rate of 7.7 ± 0.6 mm/yr. The smallest offset of a gully incised into T1 of 6.0 ± 0.5 m is potentially associated with the most recent slip event that occurred in the last millennia. The Daqing site provides a well constrained slip rate of the Haiyuan fault that is consistent with geodetic estimates. Overall, the high-resolution topography and precise chronology at the same site makes it possible to reveal the geomorphic complexities of terrace riser offsets and post-depositional evolution, and to show how previous geological rates along the fault were both under- and over-estimated.

Keywords: Haiyuan fault, northern Tibetan Plateau, slip rate, LiDAR, cosmogenic nuclide dating

INTRODUCTION

How strain is distributed in the Tibetan-Himalayan orogen is important to understand how continental orogens deform (Tapponnier and Molnar, 1977; England and Molnar, 1997). The Haiyuan left-lateral strike-slip fault, whose eastern part ruptured in 1920 AD for a length of about 230 km (Deng et al., 1984), is a major strike slip fault at the northeastern margin of the Tibetan Plateau. This fault plays an important role in accommodating eastward motion of the northern Tibet plateau relative to the Gobi-Alashan to the north (Tapponnier and Molnar, 1977; Gaudemer et al., 1995; Tapponnier et al., 2001a).

Overall, decadal geodetic and millennial geological slip-rate studies mostly agree to a rate of 4-10 mm/yr, implying that the Haiyuan fault is the major active fault at the rim of Tibet at this longitude (Li et al., 2009; Daout et al., 2016; Jiang et al., 2017). However, higher slip rates have been documented (Zhang et al., 1988a; Gaudemer et al., 1995; Lasserre et al., 1999, 2002), as well as lower ones (Yuan et al., 1998; Li et al., 2009; He et al., 2010; Jiang et al., 2017; Matrau et al., 2019). Because it has been suggested that the fault slip rate might vary over time, thus, it is valuable to find multiple slip-rate constraints at a single site to constrain possible temporal slip-rate variation (e.g., Sieh and Jahns, 1984; Van der Woerd et al., 1998, 2002).

Terrace risers have commonly been used as markers of fault displacement to constrain slip rates along strike slip faults (e.g., Lensen, 1968; Weldon and Sieh, 1985; Berryman, 1990; Knuepfer, 1992; Van der Woerd et al., 1998, 2002; McGill et al., 2013). However, terrace risers can be seldom directly dated. One may infer displacement started to be recorded since the time of upper terrace abandonment, or upon abandonment of the lower terrace (Van der Woerd et al., 2002; Mériaux et al., 2004, 2005; Cowgill, 2007; Zhang et al., 2007). In general, the upper terrace constraints yield a minimum slip rate, while the lower terrace constraint yields a maximum slip rate. Ideally, when terrace ages are not too different, a combination of

upper and lower age constraints may be used to bracket the riser age (Mériaux et al., 2005; Cowgill, 2007).

The precision of a late Quaternary slip rate depends upon displacement accumulation and its uncertainty, as well as the reliability of the corresponding dating (Sieh, 1981; Weldon and Sieh, 1985; Van der Woerd et al., 1998, 2006; Cowgill, 2007; Zhang et al., 2007; Cowgill et al., 2009; Gold et al., 2009; Le Béon et al., 2012; Mériaux et al., 2012). Across the Qilian Shan-Hexi Corridor, loess covers late Quaternary surface broadly. Researchers have often used optically stimulated luminescence (OSL) or radiocarbon ages of materials collected within the basal loess to date the end of terrace emplacement (e.g. Li et al., 2009; Jiang et al., 2017; Liu et al., 2018). In this area several studies indicate that loess deposition started just prior to the Holocene (~13-10 ka) (Stokes et al., 2003; Küster et al., 2006). Thus, loess deposition age is a minimum age for the terraces. Because terraces capped by loess usually consist of coarse gravels, if one could correct for the shielding effect due to loess cover, in-situ cosmogenic nuclides should be an appropriate dating method, ideally complemented by OSL and ^{14}C dating of loess capping materials (e.g., Hetzel et al., 2004, 2019; Perrineau et al., 2011).

High-resolution topographic data make it possible to image subtle landforms and deformation features due to active tectonics, and to make reproducible and precise measurements, improving understanding of rupture history and slip along faults (e.g. Hudnut et al., 2002; Oskin et al., 2007; Arrowsmith and Zielke, 2009; Zielke et al., 2010, 2015). Satellite or aerial photography offers two-dimensional imagery which is often used to trace fault line and look for offset markers (e.g., Tapponnier and Molnar, 1977; Peltzer et al., 1989; Meyer et al., 1998; Lasserre et al., 1999; Klinger et al., 2011; Middleton et al., 2016). Studies have applied Airborne Laser Scanning (ALS) data to map fault-zone features (e.g., Hudnut et al., 2002; Oskin et al., 2007; Arrowsmith and Zielke, 2009; Liu-Zeng et al., 2013), to survey coseismic surface ruptures (Oskin et al., 2012; Clark et al., 2017; Langridge et al., 2018) or to determine

paleo-earthquake slip distributions (Zielke et al., 2010, 2012; Thackray et al., 2013; Chen et al., 2015). Recently, this technique has also been used to measure the most recent rupture traces and offsets along the eastern Haiyuan fault (Chen et al., 2014, 2018; Ren et al., 2016).

Based on new high-resolution topography data and high precision dating, we revisit the Daqing site (also named Sangedun site in the study of Gaudemer et al., 1995), a location with multiple marker offsets, to reassess the slip rate of the Haiyuan Fault. We constrain the slip rate at this site with new offset measurements and a combination of absolute age dating approaches.

GEOLOGIC SETTING

The Haiyuan fault extends for ~1000 km from Hala Hu within the Qilian Shan in the west to the Liupan Shan in the east (Figure 1) (e.g., Tapponnier and Molnar, 1977; Gaudemer et al., 1995). Thermochronological data indicate that the Haiyuan fault initiated along its western section, then propagated eastward to the Liupan Shan area (Zheng et al., 2006; Duvall et al., 2013). The fault is characterized by left-lateral strike slip with oblique-slip components along some strands (Tapponnier and Molnar, 1977; Burchfiel et al., 1989; Gaudemer et al., 1995; Lasserre et al., 1999; Zhang et al., 1988a). Six major 70 to 300 km-long sections are distinguished and delimited by major step-overs or branches (Figure 1). Half-way along the Haiyuan fault, a major branch, the Gulang-Zhongwei fault, splays off the Haiyuan fault at the junction of the Lenglong Ling and Jinqiang He sections. It turns back towards the Haiyuan fault east of 106ºE in the Liupan Shan section. Large historical earthquakes, such as the 1709 AD Zhongwei M7.5, the 1920 AD Haiyuan Mw7.8-8.3 and the 1927 AD Gulang M8.0 earthquakes, ruptured these two faults (Deng et al., 1984; Gaudemer et al., 1995).

Several field studies along the Haiyuan fault have been carried out during the last 30 years. For instance, paleoseismic investigations along the Haiyuan (e.g. Zhang et

al., 1988b, 2003; Ran et al., 1997; Xiang et al., 1998; Min et al., 2001; Liu-Zeng et al., 2015) and Maomao Shan (e.g. Yuan et al., 1998; Liu-Zeng et al., 2007) sections show that earthquakes can rupture single or several sections together, and cluster temporally. High-resolution deposition sequences in trenches also provided evidence of magnitude 6 to 7 earthquakes (Liu-Zeng et al., 2015). Six events are documented on the Lenglong Ling section from which the most recent may be related the 1927 Gulang M8.0 earthquake (Guo et al., 2019; Gaudemer et al., 1995).

Geological slip rates determined along the Haiyuan fault differ greatly, from a few mm/yr to more than 1 cm/yr, due to different dating approaches and slip reconstruction models. For example, Lasserre et al. (2002) proposed a slip rate for the Lenglong Ling segment based on a ~200 m offset of a lateral moraine dated with cosmogenic radionuclide (CRN) of 19 ± 5 mm/yr with a lower bound of 11 ± 3 mm/yr. Along the same Lenglong Ling section, He et al. (2000) argued for a lower slip rate of 3.3-4.1 mm/yr based on older OSL dates. Recently, Jiang et al. (2017) estimated a left-lateral slip rate of 6.6 ± 0.3 mm/yr along the eastern section of the Lenglong Ling segment based on late Pleistocene ^{14}C and OSL ages of stream offsets. Along the Maomao Shan segment, Lasserre et al. (1999) determined a slip rate of 12 ± 4 mm/yr, while Yuan et al. (1998) estimated lower slip rates of 4.1-5.4 mm/yr. Yao et al. (2019) recently reassessed the offsets and age control for sites of Lasserre et al. (1999) and updated the slip rate here to 5-8.9 mm/yr over the late Pleistocene – Holocene. Further east, the Haiyuan segment, which ruptured in the 1920 Haiyuan earthquake, was assigned a slip rate of 8 ± 2 mm/yr by Zhang et al. (1988b). Li et al. (2009) updated this value to ~4.5 ± 1 mm/yr by dating offset alluvial terraces. Combining ^{10}Be CRN ages from surface and subsurface depth profiles in a set of terraces, Matrau et al. (2019) constrained a minimum slip rate of 3.2 ± 0.2 mm/yr along one of the fault strands crossing the Hasi Shan restraining bend, within the western section of the 1920 Haiyuan earthquake rupture.

157 The Jinqiang He section (3) and the Maomao Shan section (4) are nearly parallel
158 and linked across a 6 km-wide left step by a N45°E-striking and east dipping normal
159 fault, which bounds the Tianzhu half-graben or pull-apart basin in the west
160 (Gaudemer et al., 1995; Figure 2). The Jinqiang He section fault of striking N110°E
161 offsets alluvial fans and ridges along the northern side of the Jinqiang He valley.
162 There is no evidence of large earthquake during at least the past eight centuries along
163 these two fault sections, which are considered together as "the Tianzhu seismic gap"
164 (Gaudemer et al., 1995).
165 The site of Daqing (or Sangedun site in Gaudemer et al., 1995; Tapponnier et al.,
166 2001b) is located along the eastern part of the Jinqiang He section, north of the
167 Honggeda village, and ~80 km east of the sites investigated by Lasserre et al. (2002)
168 (Figure 2). The mountain range immediately to the north is locally called Leigong
169 Shan, with the highest peak reaching 4326 m. Traces of the last glaciation, in the form
170 of fresh glacial cirques, are preserved above 3700 m on the southern flank of the
171 mountain range (Gaudemer et al., 1995). Streams incising the steep southern flank of
172 the mountains feed boulder-bearing fluvio-glacial fans that are cut near the apex by
173 the Haiyuan fault. Here, glacial moraines are absent, but to the west in the Lenglong
174 Ling area, glacial landforms are common (Meyer et al, 1998; Lasserre et al., 2002;
175 Owen et al., 2003). OSL and CRN ages of glacial deposits in the Lenglong Ling area
176 indicate that the Last Glacial Maximum (LGM) took place at 18-21 ka, in agreement
177 with the timing of global LGM (Owen et al., 2003; Wang et al., 2013). Following the
178 cold and arid glacial period, fans and terraces are emplaced in the late Pleistocene and
179 early Holocene, due to increase runoff and glacial melting as the climate became
180 warmer (e.g., Meyer et al., 1998; Van der Woerd et al., 2002; Hetzel, 2013). Climatic
181 index analysis at a site on the northern flank of the Leigong Shan suggested that it
182 was warm and wet in the early Holocene (9.6-9.0 ka B.P.), and the most arid period
183 during the Holocene occurred between 9.0-8.7 ka B.P., when loess was deposited at
184 the site (Wu et al., 1998). At a regional scale, loess deposition was common but

185 spatially unevenly distributed in the Qilian Shan during the Holocene (Meyer et al.,
186 1998; Küster et al., 2006; Zhang et al., 2015).

187 At the Daqing site, a stream that flows down from a high catchment
188 (elevation >4000 m asl) and perpendicular to the main fault has abandoned a set of 3
189 main terrace levels along its west bank (Figure 3). The terraces are cut and offset by
190 the Haiyuan fault. Based on fieldwork, aerial-photo interpretation, and topographic
191 leveling with a theodolite, Gaudemer et al. (1995) determined that the three main
192 terraces are respectively offset horizontally by 143 m, 89 m, and 35 m and vertically
193 by 18 m, 11 m, and 4 m. Assigning an abandonment age of 13.5 ± 2 ka to the highest
194 terrace based on the assumption that it was deposited and abandoned during the wetter
195 and warmer period following the last glacial maximum, they proposed a slip-rate of
196 11 ± 4 mm/yr.

197

198 ## LEVELING AND GEOCHRONOLOGY METHODS

199 We used a combination of terrestrial LiDAR (TLS), Uncrewed Aerial Vehicle
200 (UAV) and kinematic GPS to survey the landforms of the Daqing site. For terrestrial
201 LiDAR, we used a Riegl VZ-1000, with an effective scan range of ~1400 m and a
202 precision of ~5 mm. Three successive scans were needed to cover all the studied area.
203 A Trimble real-time kinematic (RTK) Global Position system (GPS) surveyed the
204 position and elevation of each scanning base. These positions were used to register
205 the different point cloud datasets together. Because some places cannot be scanned by
206 the TLS due to topographic roughness, we used a DJI® Phantom 2 drone equipped
207 with a fixed focus camera to capture aerial imagery vertically and obliquely to
208 generate an ortho-photo mosaic of the site by Structure-from-Motion techniques (e.g.
209 James and Robson, 2012; Bemis et al., 2014) (Figures 3 and 4). The drone took more
210 than 120 photos at a height of about 50 m above ground surface. The flight paths are
211 parallel to the fault trace with a swath of 30-50 m. We set up 6 ground control points
212 (GCP) distributed evenly at the terrace surfaces before collecting photos. The

213 positions of GCPs were recorded by GPS-RTK. Agisoft® Photoscan was used to
214 process the aerial photos and generate the ortho-photo covering the studied site. We
215 projected the DEM derived from the TLS point cloud in the same coordinates as the
216 ortho-photo (Figures 3 and 4). Three topographic profiles were leveled in the field
217 using the Trimble RTK-GPS system described above along the various terrace risers.
218 We also extracted topographic profiles from the high-resolution DEM as single
219 profiles or swath profiles. The profiles were projected either perpendicular or parallel
220 to the fault trace (Figures 4 and 5).

221 At the Daqing site, the terrace conglomerates in the piedmont of the Leigong
222 Shan are deposited as debris flows originating from the catchment up slope. The
223 clasts within these conglomerates may have been mobilized from moraines upstream,
224 which remnants are still visible in the upper part of the catchment (Figure 3).
225 Sediments mostly comprise granite, gneiss and metasedimentary rocks. Large
226 boulders 0.5-2 m in diameter armor the surface of the terraces, some of them are
227 partially buried due to loess accumulation and soil development. Quartz-rich rock
228 samples for terrestrial cosmogenic radionuclide (CRN) dating were collected from the
229 top of boulders using chisel and hammer (Figures 4 and 6). In addition, a pit was dug
230 into the highest terrace (T3) for sub-surface sampling (Figures 4A and 7). The upper
231 1.1 m of the profile consist of 80 cm thick dark brown to black silty soil topping a 30
232 cm silty (loess) layer mixed with sparse gravels and pebbles of less than 1 cm in grain
233 size. In these upper layers we sampled 2 radiocarbon samples of bulk soil at 62 and 77
234 cm depths, and 2 OSL samples at 82 and 104 cm depths (Tables 1 and 2). In the lower
235 conglomeratic part of the profile, we collected 8 samples of amalgamated quartz-rich
236 gravels and pebbles (size < 5 cm) down to 3 m depth for cosmogenic isotope dating.
237 All sample locations were recorded using a portable GPS and elevations were
238 adjusted with the topography data from the TLS (Figure 4; Table 3).

239 Radiocarbon samples were analyzed by Beta Analytic with accelerator mass
240 spectrometry (AMS) and calibrated using Calib 7.1 (Stuiver et al., 1993) (Table 1).

The two OSL samples were processed and analyzed following Aitken (1998) and Lu et al. (2007). Coarse-grained quartz was purified from samples through chemical separation using 30% H2O2, 10% HCl, and 40% HF, and magnetic separation. The ratio of Infra-red Stimulated Luminescence (IRSL) to Blue Light Stimulated Luminescence (BLSL) has been checked to be lower than 45% to make sure the quartz is clean. A Risø TL/OSL-DA-20 reader was used for irradiation, heating and luminescence measurements (Table 2 and Figure 8). All dose rates were calculated using a central age model (Galbraith et al., 2012).

The samples analyzed for ^{10}Be cosmogenic nuclide were pre-processed at the Key Laboratory of Crustal Dynamics, China Earthquake Administration. We crushed the gravels and pebbles, purified the 250-500 μm fraction with acid leaches to obtain pure quartz, then used hydrofluoric acid to dissolve about 30 g of quartz to which a Beryllium-9 carrier solution was added. We isolated beryllium hydroxide (BeOH2) using cation exchange chromatography, which was then heated to 700°C to form beryllium oxide (BeO). Final targets were prepared at the Cosmogenic isotope Laboratory of Institut de Physique du Globe de Strasbourg (CNRS, University of Strasbourg) and processed at the ASTER-AMS facility of Centre Européen de Recherche et d'Enseignement des Géosciences de l'Environnement (Aix-en-Provence, France) for measurement (Table 3).

RESULTS

Horizontal and vertical cumulative slip determination

Combining the DEM with a resolution of ~0.1 m computed from point clouds acquired by TLS, the RTK-GPS topographic profiles, and the aerial orthophoto mosaic acquired by UAV, we produce a geomorphic map of the Daqing site (Figure 4). Overall, our mapping and leveling are consistent with previous interpretation of the site by Gaudemer et al. (1995). Three main terrace levels are abandoned and preserved on the west bank of the Daqing stream. These are offset both horizontally

and vertically due to oblique fault slip. The trace of the main Haiyuan fault can be clearly followed along the steepest part of the topographic scarp trending N110ºE. The fault trace is also marked by roughly aligned large blocks across the active stream bed, as already noted by Gaudemer et al. (1995), which are clearly visible on the aerial photo and in the field (Figure 3).

The terrace levels are well defined and separated by steep risers (Figures 4 and 5; Table 4). The terrace surfaces slope southward 14º to 8º from oldest to youngest, reflecting progressive incision and lower depositional gradient of younger deposits (Figures 4 and 5). The highest terrace level T3 is located to the west of the active riverbed. It is cut and offset by a 15-19 m-high south facing scarp. The intermediate terrace level is subdivided between older and higher standing parts, labeled T2, which are characterized by sparse outcropping boulders, and down to 6 m-deep channels, labeled T2', locally stranded by small terrace remnants designated T2'' (Figures 4 and 5). The lowest terrace level T1 stands a few meters above the active riverbed. At places, gullying and riser-slope instabilities have added some disturbance to the overall simple geomorphological setting. The height and width of the fault scarp is larger on the older terraces than on the younger ones, due to additional accumulated deformation and progressive degradation of the steep fault scarp (Figures 3 and 4) (e.g., Tapponnier et al., 1990; Zinke et al., 2015). In addition, due to relative vertical motion on the fault, terrace-riser height is larger upstream than downstream with no significant average slope change (Figure 5).

Because of lateral stream erosion and local degradation of terrace risers, terrace edges are not linear features, which lends uncertainty to reconstruction of their geometry prior of being offset. Downstream risers T3/T2' and T2/T1 are curved near the fault trace (Figures 3 and 4), which suggests that displacement of the risers started to accumulate before the lower terrace levels were completely abandoned. A number of studies have addressed the interaction between geomorphic processes and tectonic movement to determine whether terrace riser or channel offsets are true tectonic

297 offsets (e.g., Lensen, 1964; Gaudemer et al., 1989; Van der Woerd et al., 2002;
298 Cowgill, 2007; Mériaux et al., 2012; Reitman et al., 2019). To address the difficulty
299 of offset determination from geomorphic features we thus determined multiple offsets
300 for each riser, using both far- and near-field projections to the fault, and both the top
301 and bottom edges (Figure 9).

302 We determined displacement values by fitting far-field riser edges (more than
303 100 m-long and several 10s of m away from fault trace) and near-field riser edges (a
304 few 10s of m-long and near the fault trace) across the fault. Terrace risers reach up to
305 20 m height and display slopes of 10-40°, so that offsets related to riser top and
306 bottom are also specified, especially offsets of curved risers near fault trace (Figures 4
307 and 9; Table 4). It is worth pointing out that the far-field displacements of risers (e.g.,
308 D3t, D3b, D2t, D2b) are likely related to the abandonment of the adjacent upper
309 terrace, while near-field displacements (e.g., d3t, d3b, d2t, d2b) (Figure 9F) are likely
310 related to the adjacent lower terrace.

311 For the terrace riser top T3/T2', its upstream nonlinear part may be fit in two
312 ways. Either the piercing line fits tangentially the two lower convexities to the east or
313 the higher concavities to the west (Figure 4A). Downstream, the far-field piercing line
314 is perfectly linear about 60 m away from the fault. Far-field piercing lines of riser
315 base T3/T2' are almost parallel to the top on both side of the fault. Correlating riser
316 top piercing lines yield displacements of 82 ± 3 to 94 ± 3 m (this latter measurement
317 being similar to the 101.5 m of Gaudemer et al., 1995) or, on average, 88 ± 9 m.
318 Piercing lines at base of riser constrain an offset of 72 ± 3 m. The near-field riser
319 T3/T2' is curved both upstream and downstream of the fault. We can match riser top
320 (d3t) and base (d3b) with similar values of 25 ± 2 and 28 ± 2 m (Figure 4, Table 4).

321 West of T2, the eastern limit of channel T2', or the base of riser T2/T2' is only
322 determined in the near-field. Its offset of 29 ± 2 m is similar and consistent with d3b
323 (28 ± 2 m) (Figure 4, Table 4). East of T2, far-field riser top T2/T1 is linear upstream
324 of the fault and about 30 m downstream of the fault. The far-field riser base is almost

parallel to the riser top. The offsets of riser T2/T1 top and base are 35 ± 2 m and 27 ± 2 m, respectively, or on average 31 ± 4 m. The near-field riser T2/T1 is curved, particularly downstream of the fault, and its near-field riser top (d2t) and base (d2b) are similarly offset 6.5 ± 1 m (d2t and d2b, Figure 4, Table 4). A small incision in the middle of terrace T1 is also offset by 6.0 ± 0.5 m (Figures 4 and 10). Near the fault, riser T1/T0 does not preserve lateral slip, even though T1 and T0 have been ruptured in the past as indicated by the vertical offset of T1 and the visible fault trace across T0 (Figures 3C and 4). Away from the fault, the far-field riser T1-T0 seems left-laterally offset by several meters, although lateral erosion from the still active stream cannot be excluded (Figures 4 and 9).

In summary, both sets of terrace risers T3-T2' and T2-T1 show a similar pattern where far-field riser top offsets are much larger than near-field riser base offsets, 79-97 m versus 23-30 m and 33-37 m versus 5.5-7.5 m (Figure 4A). This observation suggests that far-field riser top offset ages are close to the age of the upper terrace, although it remains a maximum age and that the near-field riser base offset ages are close to the age of the lower terrace. Therefore, 88 ± 9 m can be defined as a lower bound for the horizontal offset of T3. The bounds of the offset of T2 range between 72 ± 3 m and 35 ± 2, but probably closer to the upper bound because the channel T2' offset is well constrained at 28-29 ± 2 m. Finally, the offset of T1 is well constrained at 6-6.5 ± 1 m from the similar values of the near-field riser base offset and the incision across T1 (Table 4).

In addition to left-lateral horizontal slip, the Haiyuan fault exhibits a vertical component of slip at this site (Figures 3, 4 and 5). The scarp height measured along the swath profile C1-C1' in the middle of terrace T3 (19 ± 2 m) is larger than the height from the profile C-C' following the terrace edge (15 ± 2 m) (Figures 4 and 5). This discrepancy is due to lateral displacement of the oblique slope terrace T3 relative to the fault trace (e.g., Peltzer et al., 1988; Gaudemer et al., 1995; Rodgers and Little, 2006; Chevalier et al., 2016). Correcting the measured offset of 19 ± 2 m (Vi) by

353 taking into account the slope of terrace T3 (on average 3.1° to west parallel to
354 N110°E striking fault trace, see profiles D2, E1-3 in Figure 5) and a horizontal offset
355 of 88 m yields a corrected vertical offset of 14 ± 2 m (Vr) similar to the value of 15 ±
356 2 m from the offset-riser top. Maximum slopes of terrace T2 on both sides of the fault
357 are similar and oriented perpendicular to fault trace, so that no correction is needed
358 for T2 and its vertical throw is 10 ± 1 m Figure 5, Table 4). The terrace level T2'
359 slopes on average perpendicular to the fault trace and its vertical offset ranges from
360 5.7 ± 1 m (profile B1-B1') to 6.4 ± 1 m (profile B-B'), thus on average 6.0 ± 1.5 m
361 (Figure 5, Table 4). The slopes of T1 are similar upstream and downstream and the
362 height of the fault scarp across T1 is 1.3 ± 0.2 m (Figure 5).
363 To summarize, the 4 terraces T3, T2, T2' and T1 at the Daqing site have
364 horizontal and vertical offsets of 88 ± 9 m, 33-75 m, 28.5 ± 2 m, 6.0 ± 0.5 m and 15 ±
365 2 m, 10 ± 1 m, 6.0 ± 1 m, 1.3 ± 0.2 m, respectively (Table 5). These values display a
366 consistent vertical to horizontal ratio that ranges from 0.170 to 0.211 (average 0.191 ±
367 0.018; Table 5) testifying of a constant slip vector overall (Figure 11).
368
369 **Terrace ages**
370 To constrain the age of abandonment of T3, we dug a 3 m-deep pit in the
371 downstream tread of terrace T3 (Figure 3). The upper 1.1 m of the profile exhibit a 30
372 cm sandy-loessic layer overlain by an 80 cm-thick dark brown silty soil, which partly
373 developed by incorporating wind-blown loess and sand. Below 1.1 m depth, the
374 profile penetrates the conglomeratic terrace deposit consisting of boulders, cobbles,
375 gravels and sand. Two OSL samples from the loess layer yield ages of 12.2 and 8.7 ka
376 in stratigraphic order (Figure 7, Table 2). Two radiocarbon samples from the lower
377 part of the soil yield ages of 7.7 and 7.6 ka, also in stratigraphic order (Figure 7, Table
378 1). Whether the loessic layer is of aeolian origin or reworked loess in overbank
379 deposits cannot be confirmed. In any case, the 1.1 m-thick top layer of the terrace
380 indicates deposition processes incompatible with the presence of an active stream and

thus it indicates that the underlying conglomerate has been abandoned prior to deposition of these upper layers, i.e., prior to 12.2 ka. To better constrain the age of abandonment of the terrace, we modeled the ^{10}Be concentration with depth for 8 amalgamated samples of gravel and pebbles collected from the conglomeratic terrace deposit (Figure 7, Table 3). To take into account the shielding effect of the loess and soil we propose 3 end-member models (Figure 12A). The first one (model 1) is a maximum-shielding or maximum-age model, for which despite knowledge of the loess and soil ages from other methods (OSL and ^{14}C), we consider that loess and soil were deposited immediately after the abandonment of the conglomerate forming T3 (Figure 12A). Considering the respective density of 2.0 for sandy-loess and of 1.2 for soil, the best fit of the ^{10}Be data is obtained with an exposure age of 21.6 ± 4.6 ka ($t_{1\text{-}1}$) (Figure 12D). Clearly, given the age of the lowermost OSL sample of 12.2 ka, this age is not realistic and implies stepwise or progressive emplacement of the sandy-loess and soil layers, which we consider in the following models. A second model (model 2) takes into account the oldest ages of the sandy-loess and soil deposit as the moment when these layers were deposited (Figure 12B). This model has thus 3 exposure phases, a first one corresponding to the abandonment of the conglomerate without shielding (between $t_{2\text{-}1}$ and $t_{2\text{-}2}$); a second one, with 30 cm of sandy-loess shielding starting at 12.2 ka ($t_{2\text{-}2}$); and a third one, with the additional 80 cm of soil shielding starting at 7.7 ka ($t_{2\text{-}3}$). The sandy-loess and soil layers are assumed to have been deposited instantaneously. Model 2 gives a time of exposure of the conglomerate without shielding of 2.7 ka, thus an abandonment age of 14.9 ka ($t_{2\text{-}1}$) (Figure 12E). A third model (model 3), is similar to model 2 but instead of considering an instantaneous deposition of the sandy-loess and soil layers, it considers progressive deposition of the shielding layers: 30 cm of loess deposited between 12.2 ka and 7.6 ka, (6.5 cm/ka) and 80 cm-thick soil deposited between 7.6 ka until today (10.5 cm/ka) (Figure 12C). Model 3 is a minimum shielding model or minimum age model and gives an abandonment age of 13.7 ka ($t_{3\text{-}1}$). The result of the third model is compatible

409 with all age data, and we thus suggest an abandonment age for terrace T3 of 13.7 ±
410 1.5 ka (Figure 12F).

411 For terraces T2 and T1, we collected surface exposure samples made of pieces of
412 the top of large, 0.8 to 2 m in diameter, well embedded boulders (Figures 4 and 6,
413 Table 3). As visible on sample field views in Figure 6, the boulders are variable in
414 size, in height above soil surface and also in overall shape ranging from well-rounded
415 to angular. Despite inspection of the boulders it cannot be ascertained that they have
416 not suffered alteration or spallation. We thus sampled a large number of boulders and
417 selected the best-preserved parts at the top of the boulders (Figure 6, Table 3). Seven
418 samples were collected on terrace T2 south of the fault; six samples were collected on
419 terrace T1, three to the north and three to the south of the fault (Figure 4, Table 3).
420 Both ^{10}Be concentration distributions of the samples collected on T2 and T1 indicate a
421 large scatter in the data, with overlapping values between terraces (Figure 12G). This
422 scatter may be related to unevenly distributed and large inheritance among the
423 boulders and/or variable erosion affecting the protruding large boulders at the surface
424 of the terraces (e.g., Ritz et al., 2006; Ryerson et al., 2006; Le Dortz et al., 2011).
425 Such ^{10}Be concentration scatter is a common feature of boulders originating from
426 small size high-mountain glacial catchments where accumulation and transport vary
427 with climate changes (e.g., Putkonen and Swanson, 2003; Heimsath and McGlynn,
428 2008; Heyman et al., 2011). Boulders may have sat at various depths in moraines
429 upstream at high elevation during a large part of the Pleistocene, before being
430 transported episodically, thanks to increased moist periods and during brief flash
431 floods. Unlike large catchments with deep valley fill, most of the conglomerate
432 forming part of fans and terraces at the outlet of the upper valley across the fault zone
433 were probably never buried deep enough to be shielded completely from cosmic rays.
434 The deepest gravels in the T3 depth profile have concentrations representing about 20
435 to 30% of the surface samples, which represent a significant amount of inherited ^{10}Be
436 acquired upstream. This amount of inheritance may be indicative of the intermittent

stream dynamics and evidence of sediment accumulation in the catchment. Inheritance may be distributed differently in amalgamated gravels and large boulders, as their mode of transport and residence time in the catchment differ greatly (e.g., Benedetti and Van der Woerd, 2014; Carretier et al., 2015). Assuming that the scatter is due to inheritance, the boulders with minimal inheritance are thus closest to the true surface age (e.g., Le Dortz et al., 2011; Owen et al., 2011; Prush and Oskin, 2020). For terrace T2, sample HGD14-27 has the lowest ^{10}Be concentration and an exposure age of 11.8 ± 1.1 ka. (Figure 12G, Table 3). Note that this age is younger but close to the age of the upper terrace T3 (13.7 ± 1.5 ka) and may be considered a maximum age. Additional age constraints for T2 may be given by radiocarbon dates of the overlying soil from the study of Liang et al. (2018). The ages obtained in two pits in the top soil of terrace T2 upstream and downstream of the fault indicate that T2 must have been abandoned before 9.3 ± 0.6 ka (Figure 4, Table 1). Thus, the age of terrace T2 may be bracketed between 9.3 ± 0.6 and 11.8 ± 1.1 ka.

For terrace T1, the scatter in ^{10}Be data of the 6 surface samples is similar as for terrace T2, but the range of concentrations is lower. Making similar assumptions about the origin of the scatter, the sample with the lowest ^{10}Be concentration should be close to the true age of the terrace. The lowest concentrated sample is HGD14-23 with an exposure age of 1.2 ± 0.1 ka (Figure 12G, Table 3). In the absence of better age constraints, we assume that the age of terrace T1 is close to 1.2 ± 0.1 ka.

Slip rate

Dividing the lower bound of the cumulative displacement of terrace T3, defined by the terrace T3/T2' riser top offset of 88 ± 9 m by the abandonment age of T3 of 13.7 ± 1.5 ka yields a minimum left-lateral slip rate of 6.5 ± 1 mm/yr. The bounds of the offset of terrace T2 of 72 ± 3 m and 35 ± 2 m accumulated after 9.3 ± 0.6-11.8 ± 1.1 ka yield a rate of 5.7 ± 2 mm/yr. T2' channel offset of 28.5 ± 2 m remains undated

464 in the absence of ages for T2'. And taking the age of 1.2 ± 0.1 ka for terrace T1 and
465 its 6.0 ± 0.5 m offset yields a slip rate of 5.0 ± 0.9 mm/yr (Figure 13; Table 5).

466 The observation of a near constant slip vector at the Daqing site (Figure 11) and
467 using the better determined vertical offset of the terraces (Table 5), we may estimate
468 the age of terrace T2' from its vertical offset of 6.0 ± 1.5 m and the age of T3,
469 yielding 5.4 ± 1.0 ka. Similarly, the age of T1, vertically offset 1.3 ± 0.2 m, may
470 be estimated at about 1.2 ± 0.2 ka, concordant with our assumption that it may be
471 dated with the youngest surface boulder age (1.2 ± 0.1 ka; Table 3). The same
472 relations may be used to further constrain the loosely determined horizontal offset of
473 terrace T2, which is thus likely offset about 51 m, an offset not preserved at the
474 Daqing site, probably due to lateral erosion of the lower terrace.
475

476 # DISCUSSION AND IMPLICATION

477 **Diachronous riser formation**

478 Geologic slip rate reflects faulting behavior over the long term. Geologic rates are
479 a basic datum for understanding strain accommodation through a system of faults and
480 also one of the most important indicators for earthquake potential of a fault.
481 Considerable efforts have been devoted to determining the slip rate on active faults in
482 and around the Tibetan Plateau. Although determination of a geologic fault slip rate is
483 simple in principle, it is subject to considerable uncertainty. The difficulty lies in the
484 fact that the duration of offset accumulation is often approximated by a surrogate age.
485 Indeed, terrace risers are commonly used as offset features in slip rate determination
486 of faults in northern Tibet, including the Haiyuan, the Altyn Tagh and the Kunlun
487 faults (e.g., Peltzer et al., 1989; Meyer et al., 1996; Van der Woerd et al., 1998, 2000,
488 2002; Lasserre et al., 1999; Mériaux et al., 2004, 2005, 2012; Kirby et al., 2007;
489 Cowgill, 2007; Cowgill et al., 2009). These are erosive features, which likely form
490 diachronously, starting to record offset after the abandonment of the upper terrace and
491 sometimes before the abandonment of the lower terrace (e.g., Ryerson et al., 2006;

Harkins and Kirby, 2008; Gold et al., 2009; Mériaux et al., 2012). For a given terrace riser offset, the abandonment age of the upper terrace surface provides the maximum age of slip accumulation, thus the lower bound of the true slip rate. Accordingly, the lower terrace surface age represents the minimum age of slip accumulation and thus the upper bound of the slip rate.

Terrace riser preservation results from the interaction between river erosion and displacement by the fault. In general, a terrace riser on the left bank of a river crossing a left-lateral fault is protected, i.e., continuous left-lateral slip moves the downstream section of the riser away from the stream center and is less frequently refreshed, thus more likely to record offset before the abandonment of the lower terrace (e.g., Cowgill, 2007). On the contrary, left-lateral slip on the fault is moving the downstream part of the right bank riser toward the center and in alignment with the upstream channel. This configuration favors more frequent riser refreshment and obliteration of offset before the abandonment of the lower terrace (e.g., Van der Woerd et al., 1998; Tapponnier et al., 2001a, b). However, our investigation at the Daqing site shows incomplete riser refreshment and slip accumulation before the lower terrace is abandoned. Our mapping and offset measurements of the sequentially abandoned terrace surfaces suggest that the right-bank terrace risers, i.e., erosive side, are subject to incomplete riser refreshment and partial preservation of riser offset. Several reasons may explain this situation at the Daqing site. First, the obliquity in slip vector and the accumulation of vertical displacement on the fault induces more incision in the upstream parts of the terraces (Figures 4 and 5), increasing channeling upstream and possibly less erosion downstream. Second, the main river trunk may have reduced its width progressively with time and remained channeled on the eastern side of the terraces, thus favoring preservation of the accumulated offsets.

Upper and lower bounds of the slip rate

519 The differences between geological slip rates from previous studies along the
520 Haiyuan fault stem mainly from this uncertainty of using upper terrace surface versus
521 lower terrace surface ages as the surrogate for the true offset age of the terrace riser.
522 On one hand, Lasserre et al. (1999) reported a rate of 12 ± 4 mm/yr on the eastern
523 Maomao Shan section of the Haiyuan fault. They used the lower terrace age, i.e., the
524 minimum age for offset accumulation, thus provided an upper bound for the slip rate.
525 On the other hand, much lower slip rates were reported, such as 3.1-5.8 mm/yr on the
526 Laohu Shan section (Yuan et al., 1998; Liu et al., 2018). These lower rates are based
527 on the upper terrace surface age for slip accumulation, and thus provide a lower
528 bound of the slip rate. As the many slip-rates of the Haiyuan fault shows, studies
529 finding a rate of ≤ 5 mm/yr are mainly based on an upper terrace reconstruction. In
530 only a few cases both the upper and lower terraces were dated (Li et al., 2009; Zheng
531 et al., 2013). If the lower terrace reconstruction scenario is considered in these studies,
532 an upper bound in the range of 4.5-22 mm/yr is implied, even though this upper
533 bound is not mentioned. An objective evaluation of these two previous studies shows
534 that their authors sampled the loess cover (either OSL or ^{14}C dating) of the upper
535 terrace surface, which likely postdates the abandonment of the terrace surface. The
536 implication is that even though the upper terrace constrains the maximum age of
537 offset accumulation, the loess cover age shifts the terrace age towards lower values.
538 Therefore, several slip rates documented in previous studies have in fact larger
539 uncertainties than asserted.
540 Strictly speaking, the true slip rate of the Haiyuan fault should lie between the
541 ranges of upper and lower bounds. It is helpful to resolve the variability to explicitly
542 distinguish the lower and upper bounds when reporting the rate. At the Daqing site in
543 this study, the upper and the lower bounds of the slip rate, constrained by the offset of
544 the T3/T2 terrace riser and the respective upper and lower terrace ages, are similar,
545 6.5 ± 1 mm/yr and 7.7 ± 0.6 mm/yr. This is because the ages of T3 (13.7 ka) and T2
546 (9.3-11.8 ka) are relatively close in time.

547 The terrace riser T2/T1 offset of 35 m provides a much larger uncertainty and
548 looser constraint on the slip rate (3.3-29.1 mm/yr) (Figure 13). The contrast in slip
549 rates bracketed by T3/T2 and T2/T1 at the same site highlights again that one should
550 not favor the upper or the lower terrace reconstruction scenarios, without additional
551 information. If we use the upper terrace age as the offset age, the offset of T3/T2 riser
552 suggests a slip rate of 6.5 mm/yr (since 13.7 ka), whereas the offset of T2/T1 riser
553 suggests 3.3 mm/yr (since 9.3-11.8 ka), only half as much. This difference at the same
554 site could be interpreted as a temporal change in slip rate, as has been suggested
555 elsewhere for the Haiyuan or other faults (e.g., Weldon et al., 2004; Gold et al., 2011b,
556 2017a; Liu et al., 2018). In reality, the rates may be simply the lower and upper
557 bounds, rather than the true slip rates. The rate difference may be an indication of the
558 variable initiation time of riser offset record after the abandonment of the upper
559 terrace, thus the uncertainty in slip rate determination, rather than an indication of
560 temporal change in slip behavior. Comparison between short- and long-term slip rates
561 for a number of large strike-slip faults globally suggests that the slip rate does not
562 change significantly through time (Cowgill et al., 2009; Meade et al., 2013; Tong et al,
563 2014).
564
565 **Reducing uncertainty in slip rate estimate from terrace riser offsets**
566 Terrace riser offsets may be measured in several ways to reduce uncertainties in
567 slip rate. Although we can adopt both upper and lower terrace models to bracket a
568 conservative slip rate range instead of seeking a true rate (Cowgill, 2007; Cowgill et
569 al., 2009), large differences in the ages of the upper and lower terrace can produce
570 wide range of slip rates (e.g., Mériaux et al., 2012; Gold et al., 2017b). One way of
571 reducing the uncertainty in slip rate is to lower the uncertainty in displacement bounds.
572 In general, one measures offset riser paired tops (e.g., Hubert-Ferrari et al., 2002;
573 Rizza et al, 2011; Gold et al, 2011a) or middle parts (e.g., Mason et al., 2006; Carne
574 et al, 2011) because of poor preservation of riser bases, which are locations of debris

575 accumulation (Stewart et al., 2018), or use full displacement range from top, middle
576 and base of riser (Gold et al, 2017b). In all cases, dividing such displacements by the
577 ages of the lower terraces yields the high upper bounds of the slip rate.

578 The offset of the riser base is sometimes smaller than the offset of the riser top,
579 like at our Daqing site and observed elsewhere (e.g., Gold et al. 2017b). In this case,
580 rates determined by correlating the offset riser top and base with the ages of the upper
581 and lower terraces, respectively, are more consistent, implying a vertical diachronicity.
582 As illustrated in Figure 9G, the near-field offset is preserved after abandonment of the
583 lower terrace when the stream has not totally refreshed the riser. The age of the lower
584 terrace is close to or older than the time when the near-field displacement starts to
585 accumulate. The rate between the near-field offset and the age of the lower terrace
586 abandonment may be close to the true slip rate although strictly a lower bound (e.g.
587 Mason et al., 2006; Zinke et al., 2017).

588 The advantage of multiple paired offset terraces to resolve such issues has long
589 been demonstrated (e.g., Lensen, 1964; Sieh and Jahns, 1984; Weldon, 1986;
590 Gaudemer et al, 1995; Van der Woerd et al., 1998, 2002). Considering a set of
591 independently determined slip-rates at a single site makes it possible to average the
592 variability of river incision or lateral erosion with time. At the Daqing site, the set of 4
593 terrace levels allow such approach. In our study, due to difficulties in determining the
594 precise age of all the terrace levels, we nevertheless constrained their relative ages
595 using one well-determined terrace age and their respective horizontal and vertical
596 offsets.

597 Finally, to avoid the ambiguity in correlating terrace surface ages with their
598 upper or lower risers, the offset of the terrace itself may be determined (e.g., Lensen,
599 1964; Peltzer et al., 1988, 2020). In general, this is possible when the terraces bear
600 particular syndepositional geomorphic markers at their surface (channels, ridges) or if
601 the terraces have specific inherited shapes (fan shapes, slopes) that enables
602 unambiguous geometric reconstructions.

603

604 **Stable slip vector with time**

605 The assumption of uniform slip rate over time implies that the average slip
606 vector should be temporally stable. Thus, the ratio of vertical and horizontal offsets
607 should also be constant for all terraces (Figure 11; Table 5). The vertical offset of 15
608 ± 2 m and the minimum horizontal offset of 88 ± 9 m on T3 imply a maximum ratio
609 of 0.170 ± 0.029. The ratios are 0.185 ± 0.068, 0.211 ± 0.05 and 0.2 ± 0.07 for T2, T2'
610 and T1, respectively. We consider an average ratio of 0.191 ± 0.018 consistent with
611 the range of ratios for the four terraces (Figure 11). This is larger than the ratio of
612 0.125 ± 0.025 estimated by Gaudemer et al. (1995) at this site, due to a determination
613 of a larger total horizontal displacement of the upper terrace (T3, 145 m) based on the
614 geometrical reconstruction of the terrace from a small number of topographic profiles.
615 Our terrace reconstruction, based on more exhaustive and high-resolution topographic
616 data, suggests a smaller total horizontal offset for terrace T3 and a larger average ratio,
617 consistent with the other terrace offsets (Table 5). When combining the ratio of 0.191
618 ± 0.018 and the vertical offset of 10 ± 1 m of T2, we can estimate the total horizontal
619 displacement of T2 to about 51 ± 10 m, an offset larger than the T2/T1 riser offset (35
620 ± 2 m), but smaller than the T3/T2' riser offset (72 ± 3 m). Although both the age and
621 horizontal offset of T2 are not well determined, the fact that a 51 m offset is not
622 preserved further supports lateral erosion of the T2/T1 riser after abandonment of T2
623 but prior to abandonment of T1.

624 Following the assumption of a temporally constant slip vector, our summary of
625 measured offsets versus corresponding ages (Figure 13) is compatible with a
626 temporally uniform strike slip rate of 5-8 mm/yr at this site (Table 5). The tightly
627 constrained age of T3 and the far-field offset of the lower riser top (solid rectangle in
628 Figure 13) strongly constrain this rate better than the other less well determined data
629 (dashed rectangles in Figure 13).

630

631 **Comparison with geodetic rates**

632 It is tempting to favor the lower bound estimates for the Haiyuan fault slip rate, as
633 it is closer to the geodetic rates from GPS data data (4-5 mm/yr; Li et al, 2009) or
634 from InSAR data (4-8 mm/yr; Cavalié et al., 2008; Jolivet et al., 2013; Daout et al.,
635 2016), as for the Altyn Tagh fault (Cowgill, 2007; Zhang et al., 2007; Gold et al.,
636 2009, 2011a). However, higher GPS or InSAR rates of 8.6 mm/yr were also reported
637 on the Haiyuan fault (Gan et al., 2007) and along the central section (Daout et al.,
638 2016). Furthermore, discrepancies between geologic and geodetic slip rate were found
639 on other faults, such as the San Andreas fault (Chuang et al, 2011; Johnson, 2013) and
640 the Lazio–Abruzzo fault zone in Central Italy (Papanikolaou et al., 2005).

641 These results remind us that the current GPS data is not targeted for optimal
642 determination of fault slip rate, because instrumented sites are still sparse, and thus
643 the strain rate across single faults must be estimated by collapsing measurements
644 within a wide (often 100 km wide) swath. When doing so, the effects of fault
645 geometry changes or fault interactions along strike are not taken into account. Overall,
646 the best determined rate at the Daqing site (6.5 ± 1 mm/yr) falls within the range of
647 geodetic rates (4-9 mm/yr) estimated for the Haiyuan fault system.

648

649 **Earthquake rupture implication**

650 The youngest faulted terrace T1 with its inferred age of 1.1 ± 0.1 ka implies that
651 the age of the most recent rupture at this site is even younger. At Daqing site, if
652 terrace T1 and the stream bed T0 experienced only one rupturing event, as also
653 speculated by Gaudemer et al. (1995), with the scarp across T0 being almost
654 completely eroded, the offset of ~6 ± 0.5 m of the abandoned stream channel present
655 on T1 and also the smallest lateral offset measured at the Daqing site may be
656 considered as representative of the coseismic lateral slip of the last event. Combining
657 the long-term slip rate of 5-8 mm/yr and this coseismic offset, the recurrence interval
658 for such event would be 1100 ± 300 a.

Previous paleoseismological work along fault segments adjacent to Jinqiang He segment concluded to similar values for large earthquake recurrence. For the Lenglong Ling section west of our site, mean Holocene recurrence intervals of 1430 ± 140 years (Jiang et al., 2017) and 1640 ± 570 years (Guo et al., 2019) are derived from trench investigations. To the east of our site, paleoseismological investigations showed that the Laohu Shan section seemingly ruptures every ~1000 years (Yuan et al., 1997; Liu-Zeng et al., 2007). However, only one event (after 3500 ± 200 years B.P.) was identified in a trench along the Jinqiang He section (Yuan et al., 1997). While more paleoseismological investigations are necessary to identify and date precisely the last large rupturing events along the Jinqiang He section of the Haiyuan fault, existing data and our inference from terrace T1 at Daqing site, concur to the occurrence of a large event in the last 1000 years and possible return times of 1000-2000 years for large earthquakes.

The Jinqiang He section is about 55 km long. If this section ruptures entirely the magnitude could reach up to Mw 7.1, or if a maximum coseismic displacement of 6 m is considered, the magnitude could reach up to Mw 7.4 according to empirical relationship between surface rupture length, maximum displacement and magnitude (Wells and Coppersmith, 1994). If the rupture breaches the 6 km wide Tianzhu stepover and propagates to the western part of the Maomao Shan section, the rupture length could reach 120 km and the maximum magnitude Mw 7.5 (Wells and Coppersmith, 1994). Although breaching such stepovers may be difficult (e.g., Wesnousky, 2006; Yıkılmaz et al., 2015), cascading stepping ruptures are not unusual (e.g., Tocheport et al., 2006; Xu et al., 2008; Hamling et al., 2017; Fletcher et al., 2014). Thus, the Jinqiang He and adjacent sections could be ripe for rupture in a future great earthquake. Precise seismic risk assessment demands further detailed paleoseismological investigations be carried out to define the rupture history along the central Haiyuan fault.

CONCLUSION

High resolution topography data derived from terrestrial LiDAR and Structure-from-Motion photogrammetry enable us to investigate in great detail of the offset features at the Daqing site along the Jinqiang He section of the Haiyuan fault. Terraces T1, T2', T2 and T3 were carefully mapped from field observations, orthophotos, and topographic data to produce a detailed geomorphic map of the site. Far- and near-field, top and base, of the various riser offsets have been measured as well as the vertical offset of the terraces. Horizontal offsets range from 6 to 97 m, vertical offsets range from 1 to 17 m. The smallest horizontal offset of 6.0 ± 0.5 m may be associated with the most recent coseismic slip. Terrestrial cosmogenic nuclides dating combined with ^{14}C and OSL dating were used to constrain the age of the highest terrace T3 at 13.7 ± 1.5 ka. Together with the total offset of terrace riser T3/T2 of 88 ± 9 m, it yields a left-lateral slip rate of 6.5 ± 1 mm/yr. The offset of 72 ± 5 m of the riser T3/T2 base, using the minimum age of the lower terrace (9.3 ± 0.6 ka), yields a rate of 7.7 ± 0.6 mm/yr. Overall these bounds bracket a geologic slip rate of 5-8 mm/yr for the Haiyuan fault that is consistent with the bounds estimated from geodetic data. Overall, compared to pre-existing geological rates, our rate falls in between the lower and higher estimates. At the Daqing site, the ratio of vertical and horizontal offsets of all terraces (about 1:5.2) is consistent with a uniform slip vector over time. The Daqing site provides an example that the right-bank terrace risers on a left-lateral fault, i.e., erosive side, are subject to incomplete riser refreshment and partial preservation of riser offsets.

ACKNOWLEDGMENTS

This work is jointly funded by the National Natural Science Foundation of China (41802228, U1839203), the Science for Earthquake Resilience of China Earthquake Administration (XH19044, XH18048), and YS has been partly supported by a grant from K.C. Wong Foundation and CNRS. YK is partly supported by China – France

PICS program from CNRS. GF-1 satellite imagery was offered by Dr. Wang Lin from Institute of Earthquake Science, China Earthquake Administration. We thank Alex Morelan and Veronica Prush in UC Davis for their advice on sample ages analysis. We are grateful to ASTER Team (G. Aumaître, D. Bourlès, and K. Keddadouche) at ASTER-CEREGE for AMS measurements. This work was financially supported by the INSU-CNRS, France and the University of Strasbourg to J. Van der Woerd for the Al and Be concentration analyses at LHyGeS and IPGS, and for 10Be/9Be and 26Al/27Al ratios measurements on the Aster AMS facility (GEREGE, Aix-en-Provence, France) supported by INSU-CNRS and IRD.

REFERENCES CITED

Aitken, M. J., 1998, Introduction to optical dating: the dating of Quaternary sediments by the use of photon-stimulated luminescence. Clarendon Press.

Arrowsmith, J R., and Zielke O., 2009, Tectonic geomorphology of the San Andreas fault zone from High Resolution Topography: an example from the Cholame Section: Geomorphology, v. 113, p. 70-81, doi:10.1016/j.geomorph.2009.01.002.

Bemis, S. P., Micklethwaite, S., Turner, D., James, M. R., Akciz, S., Thiele, S. T., and Bangash, H. A., 2014, Ground-based and UAV-based photogrammetry: A multi-scale, high-resolution mapping tool for structural geology and paleoseismology: Journal of Structural Geology, v. 69, p. 163-178.

Benedetti, L.C. and Van Der Woerd, J., 2014, Cosmogenic nuclide dating of earthquakes, faults, and toppled blocks: Elements, v. 10, no. 5, p. 357-361.

Berryman, K., 1990, Late Quaternary movement on the Wellington fault in the Upper Hutt area, New Zealand: New Zealand journal of geology and geophysics, v. 33, no. 2, p. 257-270.

Burchfiel, B.C., Quidong, D., Molnar, P., Royden, L., Yipeng, W., Peizhen, Z. and Weiqi, Z., 1989, Intracrustal detachment within zones of continental deformation: Geology, v. 17, no. 8, p. 748-752.

Carne, R.C., Little, T.A. and U Rieser, 2011, Using displaced river terraces to determine Late Quaternary slip rate for the central Wairarapa Fault at Waiohine River, New Zealand: New Zealand Journal of Geology and Geophysics, v.54, no. 2, p. 217-236, doi: 10.1080/00288306.2010.532224.

Carretier, S., Regard, V., Vassallo, R., Martinod, J., Christophoul, F., Gayer, E., Audin, L. and Lagane, C., 2015, A note on 10Be-derived mean erosion rates in catchments with heterogeneous lithology: Examples from the western Central Andes: Earth Surface Processes and Landforms, v. 40, no. 13, p. 1719-1729.

751 Cavalié, O., Lasserre,C., Doin, M.-P., Peltzer, G., Sun, J., Xu, X., Shen, Z.-K., 2008,
752 Measurement of interseismic strain across the Haiyuan fault (Gansu, China), by
753 InSAR: Earth and Planetary Science Letters, doi:10.1016/j.epsl.07.057.
754 Chen, T., Zhang, P. Z., Liu J., Li, C. Y., Ren, Z. K., Hudnut, K. W., 2014,
755 Quantitative study of tectonic geomorphology along Haiyuan fault based on
756 airborne LiDAR: Chinese Science Bulletin, v. 59, no. 20, p. 2396-2409,
757 doi:10.1007/s11434-014-0199-4.
758 Chen, T., Akciz, S.O., Hudnut, K.W., Zhang, D.Z. and Stock, J.M., 2015, Fault-Slip
759 Distribution of the 1999 Mw 7.1 Hector Mine Earthquake, California, Estimated
760 from Postearthquake Airborne LiDAR Data: Bulletin of the Seismological Society
761 of America, v. 105, no. 2A, p. 776-790.
762 Chen, T., Liu-Zeng, J., Shao, Y., Zhang, P., Oskin, M.E., Lei, Q. and Li, Z., 2018.
763 Geomorphic offsets along the creeping Laohu Shan section of the Haiyuan fault,
764 northern Tibetan Plateau: Geosphere, v. 14, no. 3, p. 1165-1186.
765 Chevalier, M.L., Leloup, P.H., Replumaz, A., Pan, J., Liu, D., Li, H., Gourbet, L. and
766 Métois, M., 2016, Tectonic-geomorphology of the Litang fault system, SE Tibetan
767 Plateau, and implication for regional seismic hazard: Tectonophysics, v. 682, p.
768 278-292.
769 Chuang, R.Y. and Johnson, K.M., 2011, Reconciling geologic and geodetic model
770 fault slip-rate discrepancies in Southern California: Consideration of nonsteady
771 mantle flow and lower crustal fault creep. Geology, v. 39, no. 7, p. 627-630.
772 Clark, K., E. Nissen, J. Howarth, I. Hamling, J. Mountjoy, W. Ries, K. Jones, S.
773 Goldstein, U. Cochran, P. Villamor, S. Hreinsdóttir, N. Litchfield, C. Mueller, K.
774 Berryman, D. Strong. 2017, Highly variable coastal deformation in the 2016 Mw
775 7.8 Kaikōura earthquake reflects rupture complexity along a transpressional plate
776 boundary: Earth and Planetary Science Letters,474, p. 334–344.
777 Cowgill, E., 2007, Impact of riser reconstructions on estimation of secular variation in
778 rates of strike-slip faulting: revisiting the Cherchen River site along the Altyn Tagh

779 Fault, NW China: Earth and Planetary Science Letters, v. 254, p. 239–255, doi:
780 10.1016/j.epsl.2006.09.015.
781 Cowgill, E., Gold, R.D., Xuanhua, C., Xiao-Feng, W., Arrowsmith, J.R. and Southon,
782 J., 2009, Low Quaternary slip rate reconciles geodetic and geologic rates along the
783 Altyn Tagh fault, northwestern Tibet: Geology, v. 37, no. 7, p.647-650.
784 Daout, S., Jolivet, R., Lasserre, C., Doin, M.P., Barbot, S., Tapponnier, P., Peltzer, G.,
785 Socquet, A. and Sun, J., 2016, Along-strike variations of the partitioning of
786 convergence across the Haiyuan fault system detected by InSAR: Geophysical
787 Journal International, v. 205, p. 536–547, ,doi:10.1093/gji/ ggw028.
788 Deng, Q., Sung, F., Zhu, S., Li, M., Wang, T., Zhang, W., Burchfiel, B.C., Molnar, P.
789 and Zhang, P., 1984, Active faulting and tectonics of the Ningxia-Hui autonomous
790 region, China: Journal of Geophysical Research, v. 89, p. 4427-4445.
791 Duvall, A.R., Clark, M.K., Kirby, E., Farley, K.A., Craddock, W.H., Li, C. and Yuan,
792 D.Y., 2013, Low-temperature thermochronometry along the Kunlun and Haiyuan
793 Faults, NE Tibetan Plateau: Evidence for kinematic change during late-stage
794 orogenesis: Tectonics, v. 32, no. 5, p. 1190-1211.
795 England, P. and Molnar, P., 1997, The field of crustal velocity in Asia calculated from
796 Quaternary rates of slip on faults: Geophysical Journal International, v. 130, no. 3,
797 p. 551-582.
798 Fletcher, J.M., et al., 2014, Assembly of a large earthquake from a complex fault
799 system: surface rupture kinematics of the 4 April 2010 El Mayor-Cucapah (Mexico)
800 Mw7.2 earthquake: Geosphere, v. 10, p. 797-827.
801 Galbraith, R.F. and Roberts, R.G., 2012, Statistical aspects of equivalent dose and
802 error calculation and display in OSL dating: an overview and some
803 recommendations: Quaternary Geochronology, v. 11, p. 1-27.
804 Gan, W., Zhang, P.Z., Shen, Z.-K., Niu, Z., Wang, M., Wan, Y., Zhou, D., Cheng, J.,
805 2007, Present-day crustal motion within the Tibetan Plateau inferred from GPS

806 measurements: Journal of Geophysical Research, v. 112, no. B8,
807 doi:10.1029/2005JB004120.
808 Gaudemer, Y., Tapponnier, P. and Turcotte, D.L., 1989, River offsets across active
809 strike-slip faults: Ann. tecton., v. 3, no. 3, p. 55-76.
810 Gaudemer, Y., Tapponnier, P., Meyer, B., Peltzer, G., Guo Shunmin, Chen Zhitai,
811 Dai Huagung and Cifuentes, I., 1995, Partitioning of crustal slip between linked,
812 active faults in the eastern Qilianshan, and evidence for a major seismic gap, the
813 'Tianzhu gap', on the western Haiyuan fault, Gansu(China): Geophysical Journal
814 International , v. 120, p. 599-645.
815 Gold, R.D., Cowgill, E., Arrowsmith, J.R., Gosse, J., Chen, X., and Wang, X.- F.,
816 2009, Riser diachroneity, lateral erosion, and uncertainty in rates of strike-slip
817 faulting: A case study from Tuzidun along the Altyn Tagh Fault, NW China:
818 Journal of Geophysical Research: Solid Earth, v. 114, no. B4, doi:
819 10.1029/2008JB005913.
820 Gold, R.D., Cowgill, E., Arrowsmith, J.R., Chen, X., Sharp, W.D., Cooper, K.M. and
821 Wang, X.F., 2011a, Faulted terrace risers place new constraints on the late
822 Quaternary slip rate for the central Altyn Tagh fault, northwest Tibet. Geological
823 Society of America Bulletin, v. 123, no. 5-6, p. 958-978.
824 Gold, R.D. and Cowgill, E., 2011b, Deriving fault-slip histories to test for secular
825 variation in slip, with examples from the Kunlun and Awatere faults: Earth and
826 Planetary Science Letters, v. 301, no. 1-2, p. 52-64.
827 Gold, R.D., Cowgill, E., Arrowsmith, J.R. and Friedrich, A.M., 2017a, Pulsed strain
828 release on the Altyn Tagh fault, northwest China: Earth and Planetary Science
829 Letters, v. 459, p. 291-300.
830 Gold, R. D., Briggs, R. W., Crone, A. J., and DuRoss, C. B., 2017b, Refining fault
831 slip rates using multiple displaced terrace risers—An example from the Honey
832 Lake fault, NE California, USA: Earth and Planetary Science Letters, v. 477, p.
833 134-146.

834 Guo, P., Han, Z., Mao, Z., Xie, Z., Dong, S., Gao, F. and Gai, H., 2019,
835 Paleoearthquakes and rupture behavior of the Lenglongling fault: Implications for
836 seismic hazards of the northeastern margin of the Tibetan Plateau: Journal of
837 Geophysical Research: Solid Earth, doi: 10.1029/2018JB016586.
838 Hamling, I.J., et al., 2017, Complex multifault rupture during the 2016 Mw7.8
839 Kaikoura earthquake, New Zealand: Science, 10.1126/science.aam7194.
840 Harkins, N., and Kirby, E., 2008, Fluvial terrace riser degradation and determination
841 of slip rates on strike-slip faults: An example from the Kunlun fault, China: Geo-
842 physical Research Letters, v. 35, no. L05406, 6 p., doi: 10.1029/2007GL033073.
843 He, W.G., Liu, B.C., Yuan, D.Y., and Yang, M., 2000, Study on the slip rate of
844 Lenglongling active fault zone: Northwestern Seismological Journal, v. 22, no. 1, p.
845 90-97 (in Chinese).
846 He, W.G., Yuan, D.Y., Ge, W.P. and Luo, H., 2010, Determination of the slip rate of
847 the Lenglongling Fault in the middle and eastern segments of the Qilian Mountain
848 active fault zone: Earthquake, v. 30, no. 1, p. 131-137 (in Chinese).
849 Heimsath, A.M. and McGlynn, R., 2008, Quantifying periglacial erosion in the Nepal
850 high Himalaya: Geomorphology, v. 97, no. 1-2, p. 5-23.
851 Heyman, J., Stroeven, A.P., Harbor, J.M., Caffee, M.W., 2011, Too young or too old:
852 evaluating cosmogenic exposure dating based on an analysis of compiled boulder
853 exposure ages: Earth and Planetary Science Letters, v. 302, p. 71–80.
854 Hetzel, R., Tao, M., Stokes, S., Niedermann, S., Ivy-Ochs, S., Gao, B., Strecker, M.R.
855 and Kubik, P.W., 2004, Late Pleistocene/Holocene slip rate of the Zhangye thrust
856 (Qilian Shan, China) and implications for the active growth of the northeastern
857 Tibetan Plateau: Tectonics, v. 23, no. 6, doi: 10.1029/2004TC001653.
858 Hetzel, R., 2013, Active faulting, mountain growth, and erosion at the margins of the
859 Tibetan Plateau constrained by in situ-produced cosmogenic nuclides:
860 Tectonophysics, v. 582, p. 1-24.

861 Hetzel, R., Hampel, A., Gebbeken, P., Xu, Q., & Gold, R. D., 2019, A constant slip
862 rate for the western Qilian Shan frontal thrust during the last 200 ka consistent with
863 GPS-derived and geological shortening rates: Earth and Planetary Science Letters,
864 v. 509, p. 100-113.

865 Hubert - Ferrari, A., Armijo, R., King, G., Meyer, B., and Barka, A., 2002,
866 Morphology, displacement, and slip rates along the North Anatolian Fault, Turkey:
867 Journal of Geophysical Research: Solid Earth, v. 107, no. B10, doi:
868 10.1029/2001JB000393.

869 Hudnut, K.W., Borsa, A., Glennie, C. and Minster, J.B., 2002, High-resolution
870 topography along surface rupture of the 16 October 1999 Hector Mine, California,
871 earthquake (Mw 7.1) from airborne laser swath mapping: Bulletin of the
872 Seismological Society of America,America, v. 92, no. 4, p. 1570-1576.

873 James, M.R., and Robson, S., 2012. Straightforward reconstruction of 3D surfaces
874 and topography with a camera: accuracy and geoscience application: Journal of
875 Geophysical Research: Earth Surface, v. 117, doi: 10.1029/2011JF002289.

876 Jiang, W., Han, Z., Guo, P., Zhang, J., Jiao, Q., Kang, S. and Tian, Y., 2017, Slip rate
877 and recurrence intervals of the east Lenglongling fault constrained by
878 morphotectonics: Tectonic implications for the northeastern Tibetan Plateau:
879 Lithosphere, v. 9, no. 3, p. 417-430.

880 Johnson, K.M., 2013, Slip rates and off-fault deformation in Southern California
881 inferred from GPS data and models. Journal of Geophysical Research: Solid Earth,
882 v. 118, no. 10, p. 5643-5664.

883 Jolivet, R., Lasserre, C., Doin, M.P., Peltzer, G., Avouac, J.P., Sun, J. and Dailu, R.,
884 2013, Spatio-temporal evolution of aseismic slip along the Haiyuan fault, China:
885 Implications for fault frictional properties: Earth and Planetary Science Letters, v.
886 377, p. 23-33.

887 Kirby, E., Harkins, N., Wang, E., Shi, X., Fan, C., and Burbank, D., 2007, Slip rate
888 gradients along the eastern Kunlun fault: Tectonics, v. 26, TC2010,
889 doi:10.1029/2006TC002033.
890 Klinger, Y., Etchebes, M., Tapponnier, P. and Narteau, C., 2011, Characteristic slip
891 for five great earthquakes along the Fuyun fault in China: Nature Geoscience, v. 4,
892 no. 6, p. 389-392.
893 Knuepfer, P.L., 1992, Temporal variations in latest Quaternary slip across the
894 Australian-Pacific plate boundary, northeastern South Island, New Zealand:
895 Tectonics, v. 11, no. 3, p. 449-464.
896 Küster, Y., Hetzel, R., Krbetschek, M. and Tao, M., 2006, Holocene loess
897 sedimentation along the Qilian Shan (China): significance for understanding the
898 processes and timing of loess deposition: Quaternary Science Reviews, v. 25, no. 1,
899 p. 114-125.
900 Lal, D., 1991, Cosmic ray labeling of erosion surfaces: in situ nuclide production rates
901 and erosion models: Earth and Planetary Science Letters, v. 104, p. 424-439.
902 Langridge, R. M., Rowland, J., Villamor, P., Mountjoy, J., Townsend, D. B., Nissen,
903 E., Madugo, C., Ries, W. F., Gasston, C., Canva, A., Alexandra E. Hatem, A. E.,
904 Hamling, I., 2018, Coseismic rupture and preliminary slip estimates for the
905 Papatea Fault and its role in the 2016 Mw 7.8 Kaikōura, New Zealand, Earthquake:
906 Bulletin of the Seismological Society of America, v. 108, no. 3B, p. 1596-1622.
907 Lasserre C.，Morel P.H.，Gaudemer Y.，Tapponnier P., Ryerson F.J., King G.C.P.,
908 Mtivier F., Kasser M., Kashgariana M., Liu Baichi, Lu Taiyi, Yuan Daoyang, 1999,
909 Postglacial left slip rate and past occurrence of M≥8 earthquakes on the western
910 Haiyuan fault, Gansu, China: Journal of Geophysical Research,Research, v. 104,
911 no. B8, p. 17633-17651.
912 Lasserre C., Gaudemer Y., Tapponnier P., Me´riaux A.-S., Woerd J.Van der, Yuan
913 Daoyang, Ryerson F. J., Finkel R. C., and Caffee M.W., 2002, Fast late Pleistocene

914 slip rate on the Lenglongling section of the Haiyuan fault, Qinghai, China: Journal
915 of Geophysical Research, v. 107, no. B11, p. 2276.
916 Le Béon, M., Klinger, Y., Mériaux, A.S., Al-Qaryouti, M., Finkel, R.C., Mayyas, O.
917 and Tapponnier, P., 2012, Quaternary morphotectonic mapping of the Wadi Araba
918 and implications for the tectonic activity of the southern Dead Sea fault: Tectonics,
919 v. 31, no. 5, doi:10.1029/2012TC003112.
920 Le Dortz, K., Meyer, B., Sébrier, M., Braucher, R., Nazari, H., Benedetti, L., Fattahi,
921 M., Bourlès, D., Foroutan, M., Siame, L. and Rashidi, A., 2011, Dating inset
922 terraces and offset fans along the Dehshir Fault (Iran) combining cosmogenic and
923 OSL methods: Geophysical Journal International, v. 185, no. 3, p. 1147-1174.
924 Lensen, G.J., 1964, The general case of progressive fault displacement of flights of
925 degradational terraces: New Zealand journal of geology and geophysics, v. 7, no. 4,
926 p. 864-870.
927 Lensen, G.J., 1968, Analysis of progressive fault displacement during downcutting at
928 the Branch River terraces, South Island, New Zealand: Geological Society of
929 America Bulletin, v. 79, no. 5, p. 545-556.
930 Li, C., Zhang, P.Z., Yin, J. and Min, W., 2009, Late Quaternary left-lateral slip rate of
931 the Haiyuan fault, northeastern margin of the Tibetan Plateau: Tectonics, v. 28, no.
932 5, doi:10.1029/2008TC002302.
933 Liang, S.M., Zheng, W.J., Chen, G., 2018, Offset distribution and slip rate of the
934 Jinqianghe fault of the Qilian–Haiyuan fault zone: Annual meeting of Chinese
935 Geoscience Union, Abastract in Chinese.
936 Liu, J.R., Ren, Z.K., Zhang, H.P., Li, C.Y., Zhang, Z.Q., Zheng, W.J., Li, X.M., Liu,
937 C.C., 2018, Late Quaternary slip rate of the Laohushan fault within the Haiyuan
938 fault zone and its tectonic implications: Chinese Journal of Geophysics, v. 61, no.
939 4, p. 1281-1297, doi: 10.6038/cjg2018L0364 (in Chinese).
940 Liu-Zeng, J., Klinger, Y., Xu, X., Lasserre, C., Chen, G., Chen, W., Tapponnier, P.
941 and Zhang, B., 2007, Millennial recurrence of large earthquakes on the Haiyuan

fault near Songshan, Gansu Province, China: Bulletin of the Seismological Society of America, v. 97, no. 1B, p. 14-34.

Liu-Zeng, J., Chen T, Zhang P. Z., Zhang H. P., Zheng W. J., Ren Z K, Liang S. M., Shen C. S., Gan W.J., 2013, Illuminating the active Haiyuan fault, China by AirborneLight Detection and Ranging: Chinese Science Bulletin, v. 58, p. 41-45, doi: 10.1360/972012-1526 (in Chinese).

Liu-Zeng, J., Shao, Y., Klinger, Y., Xie, K., Yuan, D. and Lei, Z., 2015, Variability in magnitude of paleoearthquakes revealed by trenching and historical records, along the Haiyuan Fault, China: Journal of Geophysical Research: Solid Earth, v. 120, no. 12, p. 8304-8333.

Lu, Y. C., Wang, X. L., and Wintle, A. G., 2007, A new OSL chronology for dust accumulation in the last 130,000 yr for the Chinese Loess Plateau. Quaternary Research, v. 67, no. 1, p. 152-160.

Matrau, R., Y. Klinger1, J. Van der Woerd, J. Liu-Zeng, Z. Li, X. Xu, and R. Zheng, 2019, Late Pleistocene-Holocene slip rate along the Hasi Shan restraining bend of the Haiyuan fault: implication for faulting dynamics of a complex fault system: Tectonics, doi: 10.1029/2019TC005488.

Mason, D. P., Little, T. A., and Van Dissen, R. J., 2006, Rates of active faulting during late Quaternary fluvial terrace formation at Saxton River, Awatere fault, New Zealand: Geological Society of America Bulletin, v. 118, no. 11-12, p. 1431-1446.

McGill, S.F., Owen, L.A., Weldon, R.J. and Kendrick, K.J., 2013, Latest Pleistocene and Holocene slip rate for the San Bernardino strand of the San Andreas fault, Plunge Creek, Southern California: Implications for strain partitioning within the southern San Andreas fault system for the last~35 ky: Geological Society of America Bulletin, v. 125, no. 1-2, p. 48-72.

Meade, B.J., Klinger, Y. and Hetland, E.A., 2013, Inference of multiple earthquake-cycle relaxation timescales from irregular geodetic sampling of interseismic

970 deformation: Bulletin of the Seismological Society of America, v. 103, no. 5, p.
971 2824-2835.
972 Mériaux, A.-S., Ryerson, F.J., Tapponnier, P., Van der Woerd, J., Finkel, R.C., Xu, X.,
973 Xu, Z., and Caffee, M.W., 2004, Rapid slip along the central Altyn Tagh fault:
974 Morphochronologic evidence from Cherchen He and Sulamu Tagh: Journal of
975 Geophysical Research, v. 109, B06401, doi: 10/1029/2003jb002558.
976 Mériaux, A.S., Tapponnier, P., Ryerson, F.J., Xu, X.W., King, G., Van der Woerd, J.,
977 Finkel, R.C., Li, H.B., Caffee, M.W., Xu, Z.Q., Chen, W.B., 2005, The Aksay
978 section of the northern Altyn Tagh fault: tectonic geomorphology, landscape
979 evolution, and Holocene slip rate: Journal of Geophysical Research: Solid Earth, v.
980 110, no. B4, B04404.
981 Mériaux, A.S., Van Der Woerd, J., Tapponnier, P., Ryerson, F.J., Finkel, R.C.,
982 Lasserre, C. and Xu, X., 2012. The Pingding segment of the Altyn Tagh Fault (91°
983 E): Holocene slip-rate determination from cosmogenic radionuclide dating of
984 offset fluvial terraces: Journal of Geophysical Research: Solid Earth, v. 117, no.
985 B9.
986 Meyer, B., Tapponnier, P., Gaudemer, Y., Peltzer, G., Guo, S., Chen, Z., 1996, Rate
987 of left-lateral movement along the easternmost segment of the Altyn Tagh Fault,
988 east of 96ºE (China): Geophysical Journal International, v. 124, p. 29-44.
989 Meyer, B., Tapponnier, P., Bourjot, L., Metivier, F., Gaudemer, Y., Peltzer, G.,
990 Shunmin, G. and Zhitai, C., 1998, Crustal thickening in Gansu-Qinghai,
991 lithospheric mantle subduction, and oblique, strike-slip controlled growth of the
992 Tibet plateau: Geophysical Journal International, v. 135, no. 1, p. 1-47.
993 Middleton, T.A., Walker, R.T., Parsons, B., Lei, Q., Zhou, Y. and Ren, Z., 2016, A
994 major, intraplate, normal-faulting earthquake: The 1739 Yinchuan event in
995 northern China: Journal of Geophysical Research: Solid Earth., v. 121, no. 1, p.
996 293-320.

997 Min, W., P. Zhang, Q. Deng, and F. Mao, 2001, Detailed study of Holocene
998 paleoearthquakes of the Haiyuan active fault: Geology Review v. 47, no. 1, p. 75–
999 81.
1000 Oskin, M. E., K. Le, and M. D. Strane, 2007, Quantifying fault-zone activity in arid
1001 environments with high-resolution topography: Geophysical Research Letters, v.
1002 34, no. L23S05, doi:10.1029/2007GL031295.
1003 Oskin, M.E., Arrowsmith, J.R., Corona, A.H., Elliott, A.J., Fletcher, J.M., Fielding,
1004 E.J., Gold, P.O., Garcia, J.J.G., Hudnut, K.W., Liu-Zeng, J. and Teran, O.J., 2012,
1005 Near-field deformation from the El Mayor–Cucapah earthquake revealed by
1006 differential LiDAR: Science, v.335, no. 6069, p. 702-705.
1007 Owen, L.A., Spencer, J.Q., Ma Haizhou, Barnard, P.L., Derbyshire, E., Finkel, R.C.,
1008 Caffee, M.W. and Zeng Yong Nian, 2003, Timing of Late Quaternary glaciation
1009 along the southwestern slopes of the Qilian Shan. Boreas, v. 32, p. 281-291.
1010 Owen, L.A., Frankel, K.L., Knott, J.R., Reynhout, S., Finkel, R.C., Dolan, J.F. and
1011 Lee, J., 2011, Beryllium-10 terrestrial cosmogenic nuclide surface exposure dating
1012 of Quaternary landforms in Death Valley: Geomorphology, v. 125, no. 4, p.
1013 541-557.
1014 Papanikolaou, I.D., Roberts, G.P. and Michetti, A.M., 2005, Fault scarps and
1015 deformation rates in Lazio–Abruzzo, Central Italy: Comparison between
1016 geological fault slip-rate and GPS data. Tectonophysics, v. 408, no. 1-4, p.
1017 147-176.
1018 Peltzer, G., Tapponnier, P., Gaudemer, Y., Meyer, B., Guo, S., Yin, K., Chen, Z. and
1019 Dai, H., 1988, Offsets of late Quaternary morphology, rate of slip, and recurrence
1020 of large earthquakes on the Chang Ma fault (Gansu, China): Journal of
1021 Geophysical Research: Solid Earth, v. 93, no. B7, p. 7793-7812.
1022 Peltzer, G., Brown, N.D., Mériaux, A.S.B., Van der Woerd, J., Rhodes, E.J., Finkel,
1023 R.C., Ryerson, F.J. and Hollingsworth, J., 2020, Stable rate of slip along the
1024 Karakax section of the Altyn Tagh Fault from observation of inter-glacial and post-

1025 glacial offset morphology and surface dating: Journal of Geophysical Research:
1026 Solid Earth, doi: 10.1029/2019JB018893.
1027 Peltzer, G., Tapponnier, P. and Armijo, R., 1989, Magnitude of late Quaternary
1028 left-lateral displacements along the north edge of Tibet: Science, v. 246, no. 4935,
1029 p. 1285-1289.
1030 Perrineau, A., Van Der Woerd, J., Gaudemer, Y., Liu-Zeng, J., Pik, R., Tapponnier, P.,
1031 Thuizat, R. and Rongzhang, Z., 2011, Incision rate of the Yellow River in
1032 Northeastern Tibet constrained by 10Be and 26Al cosmogenic isotope dating of
1033 fluvial terraces: implications for catchment evolution and plateau building:
1034 Geological Society, London, Special Publications, v. 353, no. 1, p. 189-219.
1035 Prush, V., and Oskin, M., 2020, A mechanistic erosion model for cosmogenic
1036 inheritance in single-clast exposure ages, Earth and Planetary Science Letters, v.
1037 535, doi:10.1016/j.epsl.2020.116066.
1038 Putkonen, J. and Swanson, T., 2003, Accuracy of cosmogenic ages for moraines:
1039 Quaternary Research, v. 59, no. 2, p. 255-261.
1040 Ran, Y., R. Duan, and Q. Deng, 1997, 3-D trench excavation and paleoseismology at
1041 Gaowanzi of the Haiyuan Fault: Earthquake Geology, v. 19, no. 2, p. 97-107(in
1042 Chinese with English abstract).
1043 Reitman, N.G., Mueller, K.J., Tucker, G.E., Gold, R.D., Briggs, R.W. and Barnhart,
1044 K.R., 2019. Offset channels may not accurately record strike - slip fault
1045 displacement: Evidence from landscape evolution models: Journal of Geophysical
1046 Research: Solid Earth, doi: 10.1029/2019JB018596
1047 Ren, Z., Zhang, Z., Chen, T., Yan, S., Yin, J., Zhang, P., Zheng, W., Zhang, H. and Li,
1048 C., 2016. Clustering of offsets on the Haiyuan fault and their relationship to
1049 paleoearthquakes: Geological Society of America Bulletin, v. 128, no. 1-2, p. 3-18.
1050 Ritz, J.-F., R. Vassallo, R. Braucher, E.T. Brown, S. Carretier, D.L. Bourlès, 2006,
1051 Using in situ-produced ^{10}Be to quantify active tectonics in the Gurvan Bogd

1052 mountain range (Gobi-Altay, Mongolia):): Geological Society of America Special
1053 Paper, v. 415, p. 87-110.
1054 Rizza, M., Ritz, J. F., Braucher, R., Vassallo, R., Prentice, C., Mahan, S., S. McGill,
1055 A. Chauvet, S. Marco, M. Todbileg, S. Demberel and D. Bourles, 2011, Slip rate
1056 and slip magnitudes of past earthquakes along the Bogd left-lateral strike-slip fault
1057 (Mongolia): Geophysical Journal International, v. 186, no. 3, p. 897-927.
1058 Rodgers, D.W. and Little, T.A., 2006, World's largest coseismic strike-slip offset: The
1059 1855 rupture of the Wairarapa Fault, New Zealand, and implications for
1060 displacement/length scaling of continental earthquakes: Journal of Geophysical
1061 Research: Solid Earth, v. 111, no. B12, doi: 10.1029/2005JB004065.
1062 Ryerson, F.J., Tapponnier, P., Finkel, R.C., Meriaux, A., Van der Woerd, J., Lasserre,
1063 C., Chevalier, M., Xu, X.W., Li, H.B. and King, G.C., 2006, Applications of
1064 morphochronology to the active tectonics of Tibet: Geological Society Of America
1065 Special Paper, v. 415, p. 61.
1066 Sieh, K.E., 1981, A review of geological evidence for recurrence times of large
1067 earthquakes (No. 4, p. 181-207). Washington, DC: American Geophysical Union.
1068 Sieh, K.E. and Jahns, R.H., 1984, Holocene activity of the San Andreas fault at
1069 Wallace creek, California: Geological Society of America Bulletin, v. 95, no. 8, p.
1070 883-896.
1071 Stewart, N., Gaudemer, Y., Manighetti, I., Serreau, L., Vincendeau, A., Dominguez,
1072 S., L. Mattéo, J. Malavieille, 2018, "3D_Fault_Offsets," a Matlab code to
1073 automatically measure lateral and vertical fault offsets in topographic data:
1074 Application to San Andreas, Owens Valley, and Hope faults: Journal of
1075 Geophysical Research: Solid Earth, v. 123, p. 815–835.
1076 doi:10.1002/2017JB014863.
1077 Stokes, S., Hetzel, R., Bailey, R.M. and Mingxin, T., 2003, Combined IRSL-OSL
1078 single aliquot regeneration (SAR) equivalent dose (De) estimates from source
1079 proximal Chinese loess: Quaternary Science Reviews, v. 22, no. 10, p. 975-983.

1080 Stone, J.O., 2000, Air pressure and cosmogenic isotope production: Journal of
1081 Geophysical Research, v. 105, p. 23753-23759.
1082 Stuiver M. and P.J. Reimer, 1993, Extended 14C data base and revised CALIB 3.0
1083 14C Age calibration program: Radiocarbon, v. 35, no. 1, p. 215-230.
1084 Tapponnier, P. and Molnar, P., 1977, Active faulting and tectonics in China: Journal
1085 of Geophysical Research, v. 82, no. 20, p. 2905-2930.
1086 Tapponnier, P., Meyer, B., Avouac, J.P., Peltzer, G., Gaudemer, Y., Shunmin, G.,
1087 Hongfa, X., Kelun, Y., Zhitai, C., Shuahua, C. and Huagang, D., 1990, Active
1088 thrusting and folding in the Qilian Shan, and decoupling between upper crust and
1089 mantle in northeastern Tibet: Earth and Planetary Science Letters, v. 97, no. 3-4, p.
1090 382-403.
1091 Tapponnier, P., Zhiqin, X., Roger, F., Meyer, B., Arnaud, N., Wittlinger, G. and
1092 Jingsui, Y., 2001a, Oblique stepwise rise and growth of the Tibet Plateau: Science,
1093 v. 294, no. 5547, p. 1671-1677.
1094 Tapponnier, P., Ryerson, F.J., Van Der Woerd, J., Mériaux, A.S. and Lasserre, C.,
1095 2001b, Long-term slip rates and characteristic slip: keys to active fault behaviour
1096 and earthquake hazard: Comptes Rendus de l'Académie des Sciences-Series
1097 IIA-Earth and Planetary Science, v. 333, no. 9, p. 483-494.
1098 Thackray, G.D., Rodgers, D.W. and Streutker, D., 2013, Holocene scarp on the
1099 Sawtooth fault, central Idaho, USA, documented through lidar topographic
1100 analysis: Geology, v. 41, no. 6, p. 639-642.
1101 Tocheport, A., Rivera, L., and Van der Woerd, J., 2006, A study of the 14 November
1102 2001 Kokoxili earthquake: History and geometry of the rupture from teleseismic
1103 data and field observations: Bulletin of the Seismological Society of America, v.
1104 96, no. 5, p. 1729-1741.
1105 Tong, X., Smith-Konter, B. and Sandwell, D.T., 2014, Is there a discrepancy between
1106 geological and geodetic slip rates along the San Andreas Fault System?: Journal of
1107 Geophysical Research: Solid Earth, v. 119, no. 3, p. 2518-2538.

1108 Van der Woerd J., F.J. Ryerson, P. Tapponnier, Y. Gaudemer, R. Finkel, A. S.
1109 Mériaux, M. Caffee, Zhao Guoguang, He Qunlu, 1998, Holocene left-slip rate
1110 determined by cosmogenic surface dating on the Xidatan section of the Kunlun
1111 Fault (Qinghai, China): Geology, v. 26, p. 695-698.
1112 Van Der Woerd, J., Ryerson, F.J., Tapponnier, P., Meriaux, A.S., Gaudemer, Y.,
1113 Meyer, B., Finkel, R.C., Caffee, M.W., Guoguang, Z. and Zhiqin, X., 2000,
1114 Uniform slip-rate along the Kunlun fault: Implications for seismic behaviour and
1115 large-scale tectonics: Geophysical Research Letters, v. 27, no. 16, p. 2353-2356.
1116 Van der Woerd, J., Tapponnier, P., J. Ryerson, F., Meriaux, A.S., Meyer, B.,
1117 Gaudemer, Y., Finkel, R.C., Caffee, M.W., Guoguan, Z. and Zhiqin, X., 2002,
1118 Uniform postglacial slip-rate along the central 600 km of the Kunlun Fault (Tibet),
1119 from 26Al, 10Be, and 14C dating of riser offsets, and climatic origin of the
1120 regional morphology: Geophysical Journal International, v. 148, no. 3, p. 356-388.
1121 Van der Woerd, J., Y. Klinger, K. Sieh, P. Tapponnier, F.J. Ryerson, and A.-S.
1122 Mériaux, 2006, Long-term slip rate of the southern San Andreas Fault from
1123 10Be-26Al surface exposure dating of an offset alluvial fan: Journal of
1124 Geophysical Research, v. 111, no. B04407, doi:10.1029/2004JB003559.
1125 Wang, X., Vandenberghe, D., Yi, S., Vandenberghe, J., Lu, H., Van Balen, R., and
1126 Van den Haute, P., 2013, Late Quaternary paleoclimatic and geomorphological
1127 evolution at the interface between the Menyuan basin and the Qilian Mountains,
1128 northeastern Tibetan Plateau: Quaternary Research, v. 80, no. 3, p. 534-544.
1129 Weldon, R. J., and K. E. Sieh, 1985, Holocene rate of slip and tentative recurrence
1130 interval for large earthquakes on the San-Andreas Fault, Cajon-Pass,
1131 Southern-California: Geological Society of America Bulletin, v. 96, p. 793-812.
1132 Weldon, R., 1986, The late Cenozoic geology of Cajon Pass: Implications for
1133 tectonics and sedimentation along the San Andreas fault [Ph. D. thesis]. Pasadena,
1134 California Institute of Technology.

1135 Weldon, R., Scharer, K., Fumal, T. and Biasi, G., 2004, Wrightwood and the
1136 earthquake cycle: What a long recurrence record tells us about how faults work:
1137 GSA today, v. 14, no. 9, p. 4-10.
1138 Wells, D., and K. Coppersmith, 1994, New empirical relationships among magnitude,
1139 rupture length, rupture width, rupture area, and surface displacement: Bulletin of
1140 the Seismological Society of America, v. 84, no. 4, p. 974–1002.
1141 Wesnousky, S. G., 2006, Predicting the endpoints of earthquake ruptures. Nature, v.
1142 444, no. 7117, p. 358-360.
1143 Wu, G.J., Pan, B.T., Guan, Q.Y., Wang, J.M., Zhao, Z.J., 1998, Climatic changes in
1144 the north piedmont of eastern Qilian mountains since 10 ka B. P.: Journal of Desert
1145 Research, v. 18, no. 3, p. 1993-200 (in Chinese with English abstract)
1146 Xiang, H.F., Guo, S.M., Zhang, B.L., Zhang, W.X, Yasutaka, I., and He, H.L., 1998,
1147 Active features of the eastern Liupanshan piedmont reverse fault zone since late
1148 Quaternary: Seismology and Geology, v. 20, no. 4, p. 321-327(in Chinese).
1149 Xu, X., Yu, G., Ma, W., Klinger, Y., and Tapponnier, P., 2008, Rupture behavior and
1150 deformation localization of the Kunlunshan earthquake (Mw 7.8) and their tectonic
1151 implications: Science in China Series D: Earth Sciences, v. 51, no. 10, p.
1152 1361-1374.
1153 Yao, W.Q., Liu-Zeng, J., Oskin, M.E., Wang, W., Li, Z.F., Prush, V., Zhang, J.Y.,
1154 Tang, M.Y., Shao, Y.X., Yuan, Z.D., Han, L.F., and Klinger, Y., 2019,
1155 Re-evaluation of the Late Pleistocene slip rate of the Haiyuan fault near Songshan,
1156 Gansu province, China: Journal of Geophysical Research: Solid Earth, v. 124, no.
1157 5, p. 5217-40.
1158 Yıkılmaz, M. B., Turcotte, D. L., Heien, E. M., Kellogg, L. H., and Rundle, J. B.,
1159 2015, Critical jump distance for propagating earthquake ruptures across step-overs:
1160 Pure and Applied Geophysics, v. 172, no. 8, p. 2195-2201.

1161 Yuan, D.Y., Liu, B.C., Lv, T.Y., He, W.G., and Liu, X.F., 1997, Palaeoearthquake
1162 features along the eastern segment of north Qilianshan active fault zone: South
1163 China Journal of Seismology, v. 17, no. 2, p. 24-31 (in Chinese).
1164 Yuan, D.Y., Liu, B.C., Lv, T.Y., He, W.G., Liu, X.F., and Gan, W.J., 1998, Study on
1165 the sectionation of the eastern section of north Qilianshan active fault zone:
1166 Northwestern Seismological Journal, v. 20, no. 4, p. 27-34(in Chinese).
1167 Zhang, J., Nottebaum, V., Tsukamoto, S., Lehmkuhl, F. and Frechen, M., 2015, Late
1168 Pleistocene and Holocene loess sedimentation in central and western Qilian Shan
1169 (China) revealed by OSL dating. Quaternary International, v. 372, p. 120-129.
1170 Zhang P., Molnar, P., Burchfiel, B. C., Royden, L., Wang, Y., Deng, Q., Song, F.,
1171 Zhang, W., and Jiao D., 1988a, Bounds on the Holocene slip rate along the
1172 Haiyuan fault, north-central China: Quaternary Research, v. 30, p. 151–164.
1173 Zhang P., Molnar, P., Weigi, Z., Qidong, D., Yipeng, W., Burchfiel, B.C., Fangmin,
1174 S., Royden, L. and Decheng, J., 1988b, Bounds on the average recurrence interval
1175 of major earthquakes along the Haiyuan fault in north-central China: Seismological
1176 Research Letters, v. 59, no. 3, p. 81-89.
1177 Zhang, P., W. Min, Q. Deng, and F. Mao, 2003, Paleoearthquake rupture behavior
1178 and recurrence of great earthquakes along the Haiyuan Fault, northwestern China:
1179 Science China, Ser. D, v. 46, p. 705–713.
1180 Zhang, P. Z., P. Molnar, and X. Xu, 2007, Late Quaternary and present-day rates of
1181 slip along the Altyn Tagh Fault, northern margin of the Tibetan Plateau: Tectonics,
1182 v. 26, no. TC5010, doi:10.1029/2006TC002014.
1183 Zheng, D. W., P. Z. Zhang, J. L. Wan, D. Y. Yuan, C. Y. Li, G. M. Yin, G. L. Zhang,
1184 Z. C. Wang, M. Min, and J. Chen, 2006, Rapid exhumation at similar to 8 Ma on
1185 the Liupan Shan thrust fault from apatite fission-track thermochronology:
1186 Implications for growth of the north- eastern Tibetan Plateau margin: Earth and
1187 Planetary Science Letters, v. 248, no. 1–2, p. 198–208.

Zheng, W.J., Zhang, P.Z., He, W.G., Yuan, D.Y., Shao, Y.X., Zheng, D.W., Ge, W.P. and Min, W., 2013, Transformation of displacement between strike-slip and crustal shortening in the northern margin of the Tibetan Plateau: Evidence from decadal GPS measurements and late Quaternary slip rates on faults: Tectonophysics, v. 584, p. 267-280.

Zielke, O., J R. Arrowsmith, L. B. Grant-Ludwig, and S. O. Akciz, 2010, Slip in the 1857 and earlier large earthquakes along the Carrizo section, San Andreas Fault: Science, v. 327, p. 1119-1122, doi:10.1126/science.1182781.

Zielke, O., J R. Arrowsmith, L. B. Grant-Ludwig, and S. O. Akciz, 2012, High resolution topography-derived offset along the 1857 Fort Tejon earthquake rupture trace, San Andreas Fault: Bulletin of the Seismological Society of America, v. 102, no. 3, doi:10.1785/0120110230.

Zielke, O., Klinger, Y. and Arrowsmith, J.R., 2015, Fault slip and earthquake recurrence along strike-slip faults—Contributions of high-resolution geomorphic data: Tectonophysics, v. 638, p. 43-62.

Zinke, R., Dolan, J.F., Van Dissen, R., Grenader, J.R., Rhodes, E.J., McGuire, C.P., Langridge, R.M., Nicol, A. and Hatem, A.E., 2015, Evolution and progressive geomorphic manifestation of surface faulting: A comparison of the Wairau and Awatere faults: South Island, New Zealand. Geology, v. 43, no. 11, p. 1019-1022.

Zinke, R., Dolan, J. F., Rhodes, E. J., Van Dissen, R., & McGuire, C. P., 2017, Highly variable latest Pleistocene-Holocene incremental slip rates on the Awatere fault at Saxton River, South Island, New Zealand, revealed by lidar mapping and luminescence dating: Geophysical Research Letters, v. 44, p. 11,301–11,310, doi: 10.1002/2017GL075048.

Figures caption:

Figure 1. (A) Active faults map of northeastern Tibetan plateau. Seismicity from 780 BC to 2006 AD. Historical earthquakes from Division of Earthquake Monitoring and Prediction, State Seismologic Bureau (1995), instrumental seismicity from China Earthquake Networks Center (http://www.cenc.ac.cn/). White star indicates study site, dashed box is figure 1B. Haiyuan fault is subdivided into six sections separated by black arrows, from west to east: (1) Halahu, (2) Lenglong Ling, (3) Jinqiang He, (4) Maomao Shan, (5) Jingtai, (6) Haiyuan, and (7) Liupan Shan. Inset is location map showing tectonic framework of the Tibetan plateau.plateau (B) Active faults along Jinqiang He section that extends from Lenglong Ling-Gulang-Jinqiang (LGH) fault triple junction to the west, to Tianzhu pull-apart basin (TB) to the east, left-stepping to Maomao Shan section. Upper Jinqiang He valley is fed mostly by north-south tributaries flowing down from Leigong Shan to the north and crossing the Haiyuan fault at high angle. LLL: Lenglong Ling.

Figure 2. GF-1 satellite imagery (pixel ~2 m) of Jinqiang He section of Haiyuan fault near Daqing site (white rectangle) upstream from Honggeda village. Light shading delimits Tianzhu half pull-apart basin.

Figure 3. (A) Uncrewed aerial vehicle (UAV) derived photo mosaic with ~0.2 m resolution of Daqing site. Fault trace is clear across stream bed T0 and terraces T1 to T3 to the west. Red arrows point to fault trace. (B) West-looking panoramic field view of faulted terraces at Daqing site. (C) Oblique close-up view showing fault trace across T0, T1 and T2.

Figure 4. (A) Geomorphic map of Daqing site from field observations, UAV photo mosaic interpretation, and high-resolution DEM analysis. Contours with 1 m interval derived from ~0.1 m resolution terrestrial LiDAR DEM. Dashed lines are topographic profiles shown in Figure 5. Pit and sample position for dating are indicated. Purple lines are terrace riser piercing lines for horizontal offset measurements. (B) Hill shading and (C) slope map of DEM highlighting terrace surface morphology, distinct terrace risers and fault scarp.

Figure 5. Topographic profiles across and along terraces at Daqing site. Locations shown in Figure 4. Gray dots are measurement points, solid black lines along slopes are fitting lines. AA', BB' and CC' are field GPS-RTK profiles, others are swath profiles extracted from LiDAR-DEM. Dashed line in swath profiles represents mean elevation value. Small sketch illustrates correction applied to apparent vertical offset of T3 due to oblique orientation of its sloping surface. Vr, corrected vertical offset, is function of Vi vertical throw measurement from perpendicular fault profile C1-C1', h

is horizontal offset of terrace, α is angle of terrace slope parallel to fault (in profiles E1, E2, E3) (see also Gaudemer et al., 1995).

Figure 6. Field photographs of surface boulders sampled for cosmogenic dating from terraces T2 (A) and T1 (B). See position in Figure 4 and analytical details in Table 3.

Figure 7. (A) Field view of samplings pit in terrace T3 (position in Figure 4). (B) Stratigraphic description of pit. Eight gravels and pebbles samples were collected from below 80 cm to 3 m depth for cosmogenic isotope dating (details in Table 3). Open circles are sandy loess samples collected for OSL dating (Table 2), solid triangles are bulk soil samples for ^{14}C dating (Table 1).

Figure 8. Equivalent dose (De) distributions, natural OSL decay curve and growth curves for samples HGDOSL-1501 (A and B) and HGDOSL-1502 (C and D), respectively.

Figure 9. Offset terrace reconstructions. (A)-(E) diagrams of different stages during river downcutting, lateral erosion and displacement accumulation. Simplified risers are vertical. (F) sketch of offset terraces at Daqing site. All measurement results are shown in Table 4. (G) shows how near-field (d3t, d3b, d2t and d2b) and far-field displacements are related.

Figure 10. Field details of smalls stream offset on terrace T1. Red arrows indicate top of fault scarp across T1.

Figure 11. Ratio of vertical to horizontal offsets. Average ratio is 0.191+/-0.018 by T3, T2, T2' and T1.

Figure 12. Exposure age constraints at Daqing site. (A), (B) and (C) are proposed stepwise evolution of deposit for terrace T3 ^{10}Be depth profile modeling in (D), (E) and (F). $t_{1\text{-}1}$, $t_{2\text{-}1}$and $t_{3\text{-}1}$ are corresponding terrace abandonment ages for models 1, 2 and 3; R-squared is statistical assessment of ^{10}Be data with respect to best fit, without outliers (black circles). Integrated density (blue line) and average inheritance indicated. (A and D) model 1: assumes all layers deposited in one step (I). (B and E) model 2: exposure in three steps: (I) terrace conglomerate only ($t_{2\text{-}1}$ - $t_{2\text{-}2}$), (II) with 30 cm-thick sandy-loess ($t_{2\text{-}2}$ - $t_{2\text{-}3}$), and (III) with 80 cm-thick soil ($t_{2\text{-}3}$ - 0). All layers are deposited instantaneously. (C and F) model 3: same as model 2 but layers are deposited progressively, as constrained by OSL and ^{14}C dates. (G) ^{10}Be concentrations of surface samples from terraces T1 (n=6) and T2 (n=7)) represented as Gaussian distributions. Scatter of distributions mostly attributed to inheritance (see

text). Samples in bold (HGD14-23 and HGD14-27) are samples with lowest ^{10}Be concentration in each distribution.

Figure 13. Summary of terrace offsets at Daqing He site as a function of age. Solid rectangle is best determined rate from terrace T3. Dashed rectangles are less well determined. Gray shaded area is preferred range of the slip rate.

TABLE 1. Radiocarbon analytical results of samples from terraces T3 and T2.

Sample	Lab [a]	Depth (m)	Fraction Modern	±	$D^{14}C$ (‰)	±	^{14}C Age (B.P.)	±	2σ calibrated age (B.P.) [b]
HGD-C14-01	414950	0.77	0.4236	0.0016	-576.4	1.6	6900	30	Cal 7790 - 7675
HGD-C14-02	414951	0.62	0.4414	0.0016	-558.6	1.6	6570	30	Cal 7555 - 7545
L-01 [c]		0.89					8630	90	Cal 9900 - 9474
L-02 [c]		0.82					8180	140	Cal 9475 - 8715

a: All samples were AMS dated at Beta Analytic;

b: Calibration with Calib 7.1 (Stuiver et al., 1993), did not include probability distribution of range < 0.1;

c: L-01, L-02 are from Liang et al. (2018), Fraction Modern and $D^{14}C$ information not known.

TABLE 2. Analytical results of OSL samples from terrace T3.

Sample No	Lab. no[a]	Depth (m)	Water content[b] (%)	U (ppm)	Th (ppm)	K (%)	Cosmic dose rate (Gy/ka)	Grain size (μm)	Dose rate [c] (Gy/ka)	Equivalent dose[d] (Gy)	Age[e] (ka)
HGDOSL-1502	15-64	0.82	2.6	2.71±0.1	14.4±0.39	2.18±0.06	0.32±0.02	90-125	4.06±0.15	35.3±1.3	8.7±0.5
HGDOSL-1501	15-63	1.04	8.04	2.45±0.1	12.8±0.36	2.12±0.06	0.31±0.02	90-125	3.61±0.13	44.2±0.8	12.2±0.5

a: All samples were processed at Zhejiang Zhongke Institute of Luminescence Testing Technology;

b: Measured water content;

c: Concentrations of U, Th and K were measured by neutron activation analysis at the China institute of atomic energy;

d: All equivalent dose values conform to normal distribution;

e: Calculated with the central age model (Galbraith et al., 2012).

TABLE 3. ^{10}Be analytical data at Daqing site

Samples	Mass quartz (g)	Be carrier (mg)	Latitude (N)	Longitude (E)	Altitude (m)	Depth (cm)	Thickness (cm)	Sample type	Height above surface/size (m)	10Be/9Be	10Be/9Be error (%)	10Be ± error (atom/g)	Exposure age ± uncertainty (yr)
Terrace T1													
HGD14-08	30.107	0.2461	37.259544	102.696663	3441	0	2.5	boulder/granite	1.2/2	1.11247E-12	3.1680	608254 ± 19269	13344 ± 1205
HGD14-09	26.9599	0.2699	37.259254	102.696609	3432	0	2.5	boulder/granite	0.5/1.3	5.23986E-13	3.0904	350879 ± 10843	7705 ± 693
HGD14-10	25.7075	0.241	37.259041	102.696503	3426	0	2.5	boulder/gneiss	1/1.5	7.61713E-13	3.1744	477641 ± 15162	10529 ± 951
HGD14-16	30.0079	0.2458	37.256313	102.695001	3369	0	2.5	boulder/granite	1.6/3.5	3.02524E-13	3.1761	165752 ± 5264	3956 ± 357
HGD14-22	29.8354	0.25	37.256969	102.695702	3389	0	2.5	boulder/granite	0.1/0.8	6.77539E-13	3.1746	379748 ± 12055	8594 ± 776
HGD14-23	29.972	0.2517	37.257381	102.695984	3393	0	2.5	boulder/granite	0.2/1.2	8.62754E-14	3.5217	48462 ± 1706	1165 ± 106
Terrace T2													
HGD14-18	30.0132	0.2901	37.255253	102.694336	3351	0	2.5	boulder/granite	0.2/0.8	1.11507E-12	3.0821	720924 ± 22219	16489 ± 1486
HGD14-19	24.5073	0.2253	33.255444	102.69445	3354	0	2.5	boulder/granite	0.2/1.1	1.41835E-12	3.4983	872173 ± 30511	21606 ± 1982
HGD14-20	30.0075	0.2495	2 m south of sample 19			0	2.5	boulder/granite	0.2/1.1	2.79689E-12	1.9939	1555499 ± 31016	36437 ± 3185
HGD14-25	30.0081	0.2555	37.256226	102.694389	3371	0	2.5	boulder/granite	0.2/1	1.37277E-12	3.0506	781814 ± 23850	17590 ± 1584
HGD14-26	25.0845	0.2432	37.257112	102.69458	3388	0	2.5	boulder/granite	0.1/1.3	1.23744E-12	3.0546	802483 ± 24512	17877 ± 1610
HGD14-27	30.0488	0.2546	37.257439	102.694618	3391	0	2.5	boulder/granite	0.5/1.5	9.21578E-13	3.1078	522297 ± 16232	11788 ± 1062
HGD14-28	30.0016	0.253	37.257252	102.69455	3393	0	2.5	boulder/gneiss	1/1.5	1.12670E-12	3.1186	635531 ± 19820	14360 ± 1295
Terrace T3 depth profile													
HGDT3-01	31.4296	0.2592	37.257061	102.693886	3389	85	5	gravels	0.02-0.05	1.30104E-12	2.4296	717695 ± 17436	See model
HGDT3-02	29.9764	0.2484	37.257061	102.693886	3389	100	5	gravels	0.02-0.05	2.05011E-12	2.6603	1136327 ± 30229	/
HGDT3-03	25.1784	0.2563	37.257061	102.693886	3389	115	5	gravels	0.02-0.05	8.73919E-13	3.1803	595039 ± 18923	/

HGDT3-04	32.0859	0.2514	37.257061	102.693886	3389	145	5	gravels	0.02-0.05	7.71630E-13	3.2954	404402 ± 13326	/
HGDT3-05	30.1135	0.2566	37.257061	102.693886	3389	175	5	gravels	0.02-0.05	5.80584E-13	3.0688	330913 ± 10154	/
HGDT3-06	29.3054	0.254	37.257061	102.693886	3389	205	5	gravels	0.02-0.05	6.24376E-13	3.0946	361981 ± 11201	/
HGDT3-07	30.0178	0.2501	37.257061	102.693886	3389	245	5	gravels	0.02-0.05	6.97878E-13	3.5702	388926 ± 13885	/
HGDT3-08	30.041	0.2549	37.257061	102.693886	3389	285	5	gravels	0.02-0.05	4.62999E-13	3.2264	262778 ± 8478	/

Note: All samples were processed at Key Laboratory of Crustal Dynamics, China Earthquake Administration and AMS measurements performed at ASTER in Centre de Recherche et d'Enseignement de Géosciences de l'Environnement (CEREGE), Aix-en-Provences, France. Surface boulder model ages for terraces T3 and T2 calculated with the CRONUS 2.3 calculator (Balco et al., 2008; http://hess.ess.washington.edu/), with Time-dependent Lal (1991) / Stone (2000) scaling scheme for spallation, with density of 2.7 and assuming no erosion and no inheritance.

TABLE 4. Terrace geometry, vertical terrace offsets and horizontal terrace riser offsets

	Marker	Parameter	Value (m)	Error (m)	Note
Tread widths	T1 upstream	W1u	61	4	
	T1 downstream	W1l	34	2	
	T2’ upstream		42	2	
	T2’ downstream west		9	2	
	T2’ downstream east		22	2	
	T2 tread	W2u	135	5	
	T2 tread	W2l	89	3	
Riser heights	T1-T0	R1u	6	1	upstream
		R1d	2.5	0.5	downstream
	T2’-T1		10-11	1	upstream
			5-6	1	downstream
	T2”-T2’		2	1	upstream
	T2-T2’		6	1	upstream
			1.5-2.5	0.5	downstream
	T2-T1	R2u	16-17	1	
		R2d	7.5	1	downstream
	T3-T2’		16-21	1	upstream
			3.1-4.2	0.5	downstream
	T3-T2	R3u	10-15	1	upstream
		R3d	1.4-1.7	0.3	downstream
Vertical terrace offsets	T1 A-A’	Sc1	1.3	0.2	slop 10°/9.5°
	T1 A1-A1’		1.3	0.2	slop 9°/9°
	T2’ B1-B1’		5.7	1	slop 8.9°/8.5°
	T2’ B-B’		6.4	1	slop 10.5°/10.5°
	T2 B1-B1’	Sc2	9	1	slop 9.9°/7.5°
	T2 B-B’		10	1	slop 10.5°/9.5°
	T3 C1-C1’	Sc3	19	2	slop 11.7°/7.5°
	T3 C-C’		15	2	slop 13.7°/9.5°
Horizontal riser offsets	Stream	Ds	6.0	0.5	
	T2/T1	D2t	35	2	
		D2b	27	2	
		d2t	6.5	1	
		d2b	6.5	1	
	T3/T2	D3t	94	3	
			82	3	
		D3b	72	3	
		d3t	25	2	
		d3b	28	2	
	T2’	d2’b	29	2	

West bank 28 2

TABLE 5. Summary of slip rates at Daqing site

	T1	T2’	T2	T3	Average
Horizontal offset (m)	6.5 ± 1	28.5 ± 2	35 ± 2-72 ± 3/(54 ± 19)	>88 ± 9	
Vertical offset (m)	1.3 ± 0.2	6 ± 1.5	10 ± 1	15 ± 2	
Ratio (Vertical/ Horizontal)	0.2 ± 0.07	0.211 ± 0.05	0.185 ± 0.068	<0.170 ± 0.029	0.191 ± 0.018
Age (ka)	<1.2 ± 0.1 (bound)	5.4 ± 1 (estimated)	9.3±0.6-11.8 ± 1.1 (bounds)	13.7 ± 1.5	
Horizontal slip rate (mm/yr)	>5 ± 0.9	5.5 ± 1.4	5.7 ± 2	> 6.5 ± 1	5-8
Vertical slip rate (mm/yr)	>1.1 ± 0.2	1.1 ± 0.5	1 ± 0.3	1.1 ± 0.3	1.1 ± 0.3

Figure 1

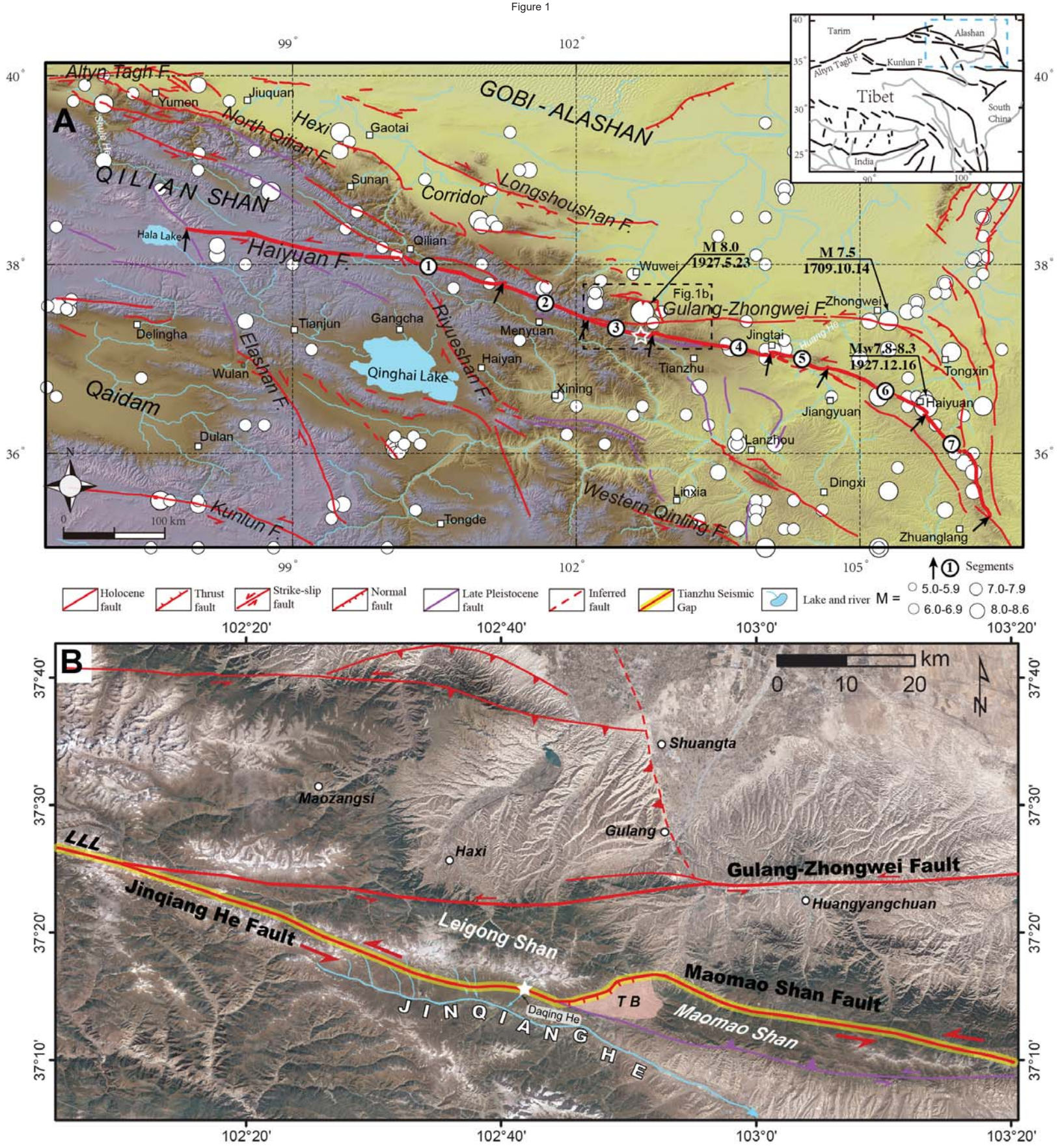
A
Altyn Tagh F.
Yumen
Jiuquan
Hexi
North Qilian F.
GOBI - ALASHAN
Gaotai
Sunan
Corridor
Longshoushan F.
QILIAN SHAN
Hala Lake
Haiyuan F.
Qilian
Wuwei
M 8.0
1927.5.23
M 7.5
1709.10.14
Fig.1b
Gulang-Zhongwei F.
Zhongwei
Tianjun
Gangcha
Riyueshan F.
Menyuan
Delingha
Elashan F.
Haiyan
Qinghai Lake
Jingtai
Huang He
Mw7.8-8.3
1927.12.16
Tianzhu
Tongxin
Wulan
Xining
Qaidam
Jiangyuan
Haiyuan
Dulan
Lanzhou
Dingxi
Linxia
Western Qinling F.
Kunlun F.
Tongde
Zhuanglang
Tarim
Alashan
Altyn Tagh F
Kunlun F
Tibet
South China
India
99°
102°
105°
40°
38°
36°
0
100 km
Holocene fault
Thrust fault
Strike-slip fault
Normal fault
Late Pleistocene fault
Inferred fault
Tianzhu Seismic Gap
Lake and river
M =
5.0-5.9
6.0-6.9
7.0-7.9
8.0-8.6
Segments

B
km
0
10
20
N
Shuangta
Maozangsi
Gulang
Haxi
LLL
Gulang-Zhongwei Fault
Huangyangchuan
Jinqiang He Fault
Leigong Shan
Maomao Shan Fault
TB
Maomao Shan
Daqing He
JINQIANG HE
102°20'
102°40'
103°0'
103°20'
37°40'
37°30'
37°20'
37°10'

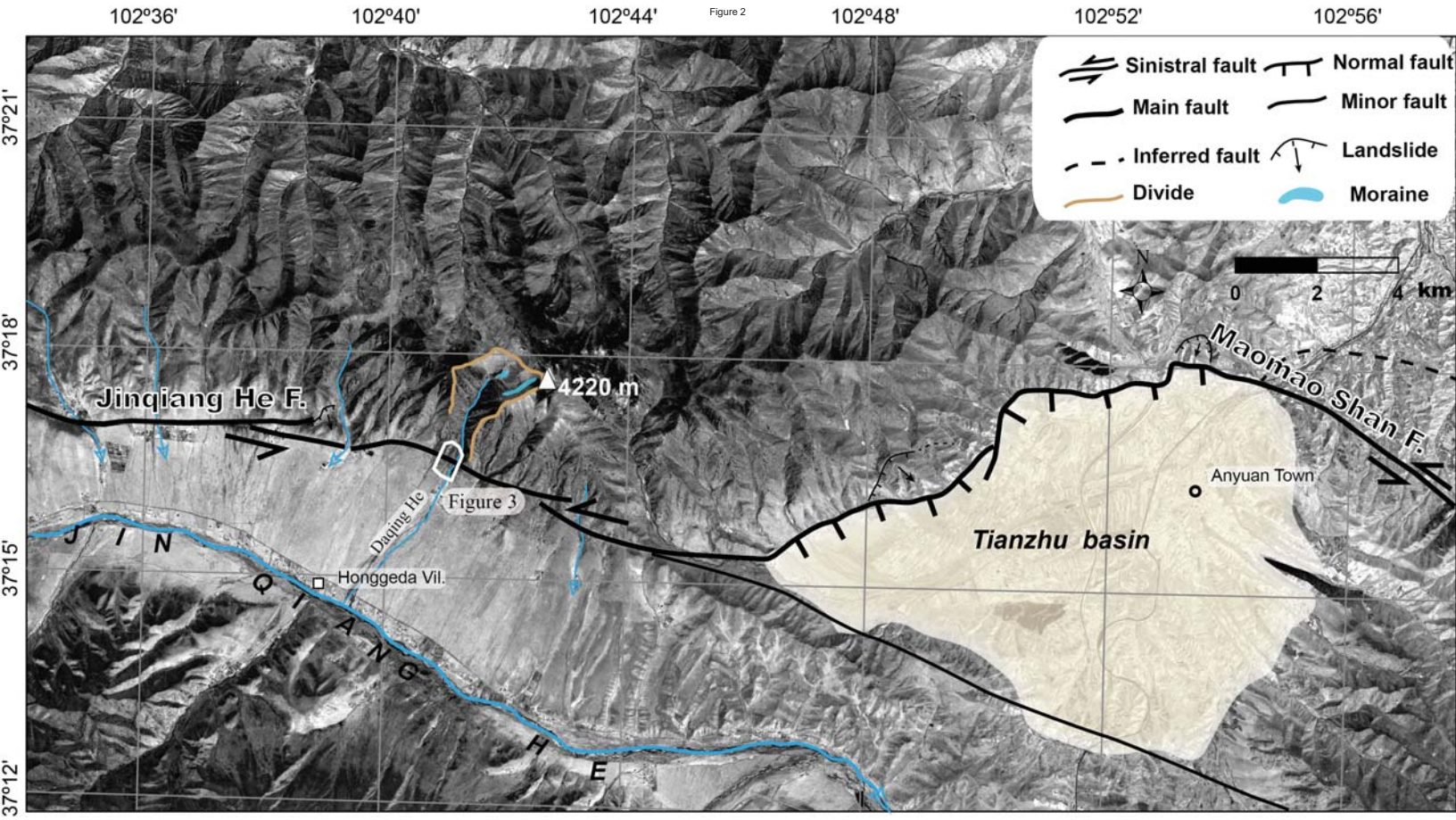
102°36'
102°40'
102°44'
102°48'
102°52'
102°56'
37°21'
37°18'
37°15'
37°12'
Sinistral fault
Normal fault
Main fault
Minor fault
Inferred fault
Landslide
Divide
Moraine
N
0
2
4 km
Jinqiang He F.
4220 m
Maomao Shan F.
Anyuan Town
Figure 3
Daqing He
Tianzhu basin
Honggeda Vil.
JINQIANG HE

Figure 2

Figure 3

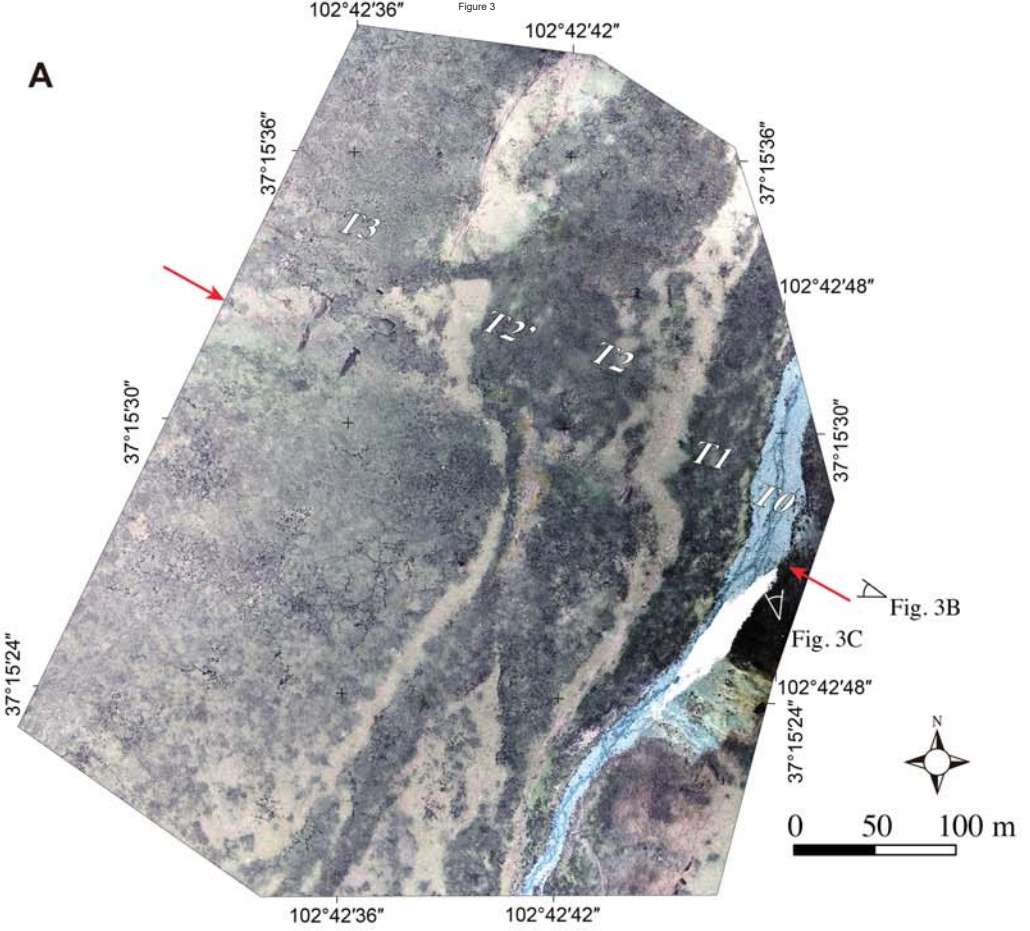
A
102°42'36"
102°42'42"
37°15'36"
37°15'30"
37°15'24"
102°42'48"
T3
T2'
T2
T1
T0
Fig. 3B
Fig. 3C
N
0 50 100 m


B
T3
T2'
T2
T1
T0


C
T2
T1
T0
S
N

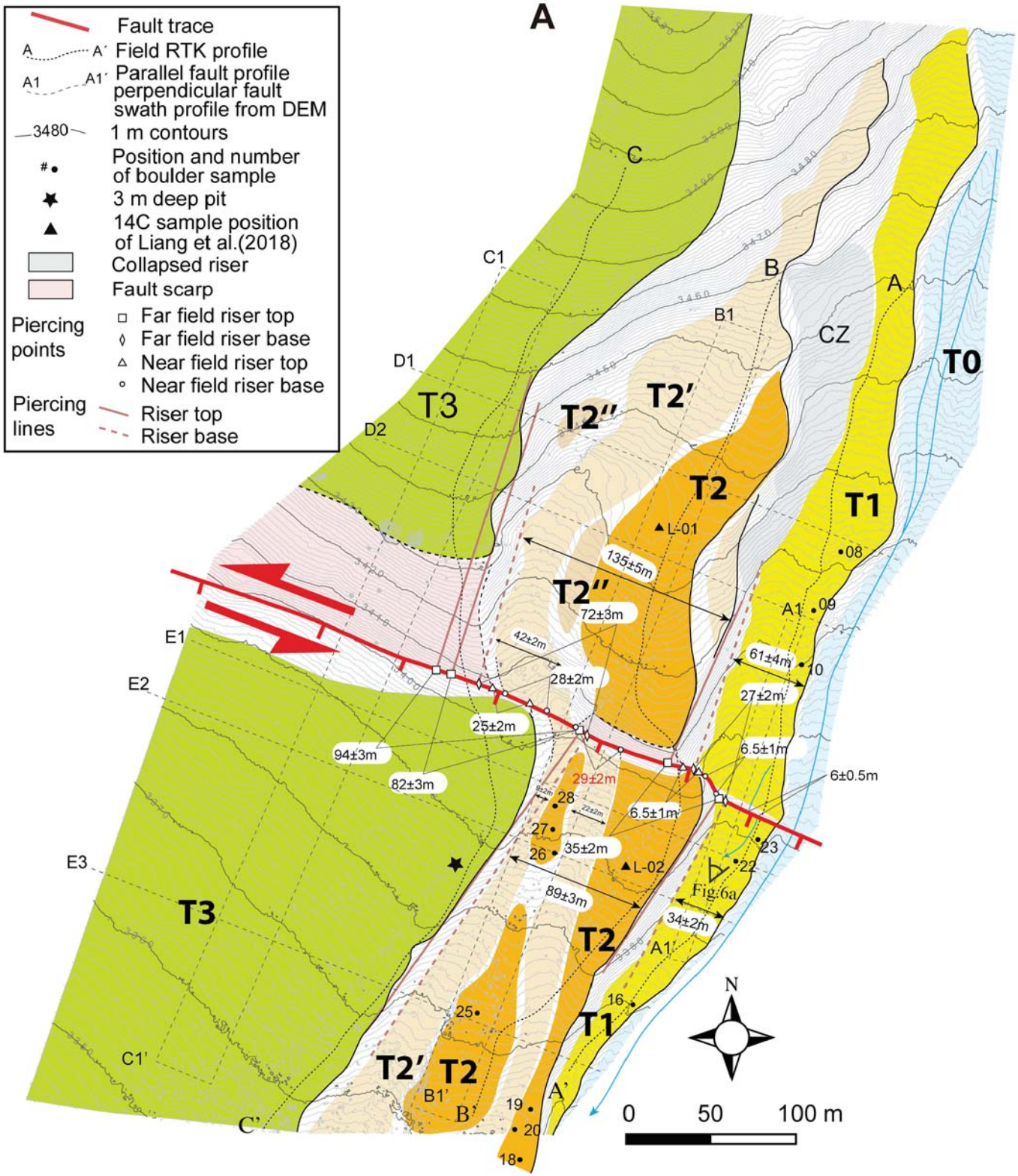
A
Fault trace
A A' Field RTK profile
A1 A1' Parallel fault profile perpendicular fault swath profile from DEM
3480 1 m contours
Position and number of boulder sample
3 m deep pit
14C sample position of Liang et al.(2018)
Collapsed riser
Fault scarp
Piercing points
Far field riser top
Far field riser base
Near field riser top
Near field riser base
Piercing lines
Riser top
Riser base
C
C1
D1
D2
E1
E2
E3
C1'
C'
B
B1
B1'
B'
A'
A1
A1'
CZ
T0
T1
T2
T2'
T2"
T3
L-01
L-02
135±5m
72±3m
42±2m
28±2m
25±2m
94±3m
82±3m
29±2m
6.5±1m
35±2m
89±3m
61±4m
27±2m
6.5±1m
6±0.5m
34±2m
08
09
10
22
23
Fig.6a
N
0 50 100 m
Figure 4A

Figure 4B C

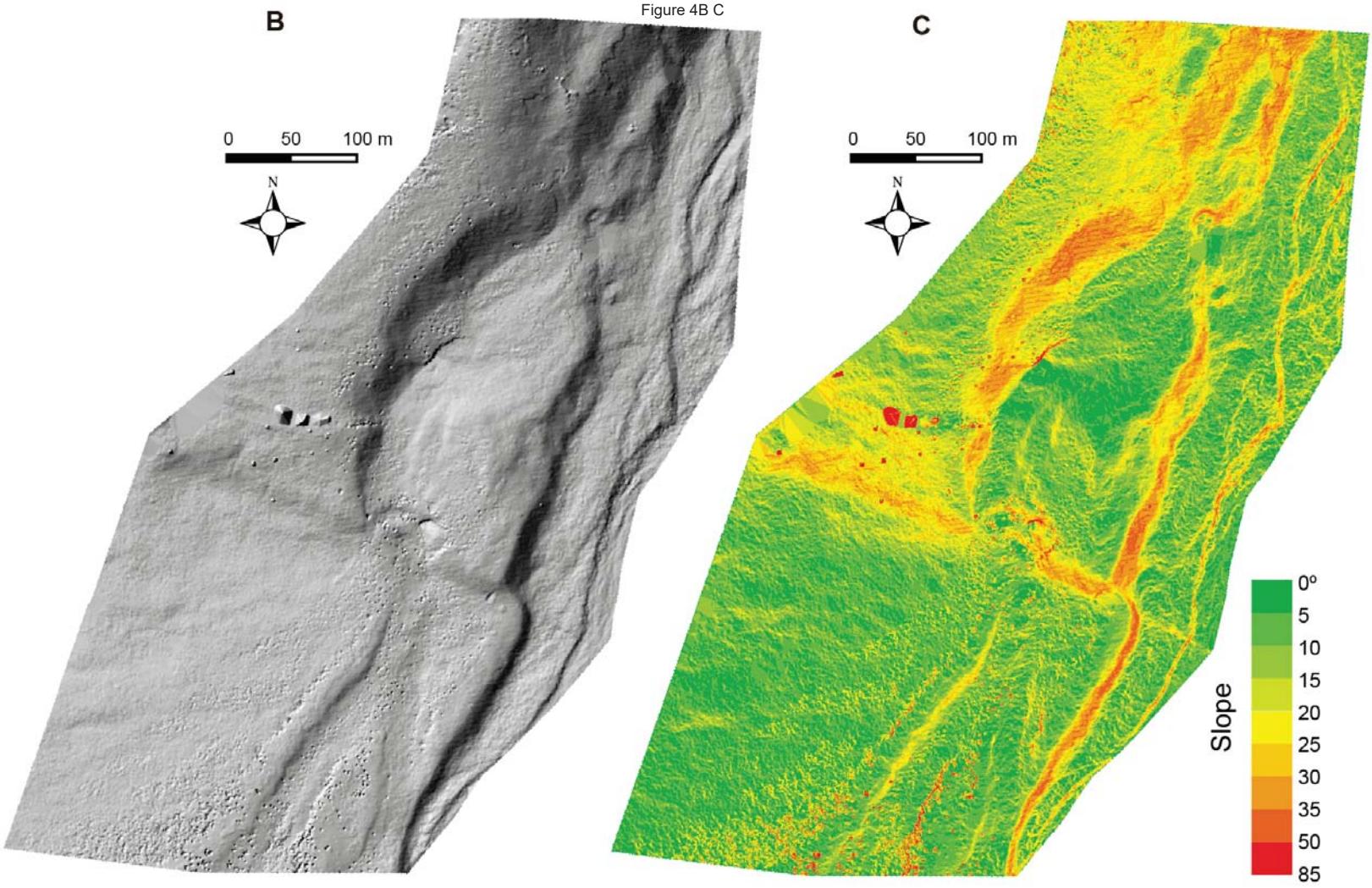

Figure 5

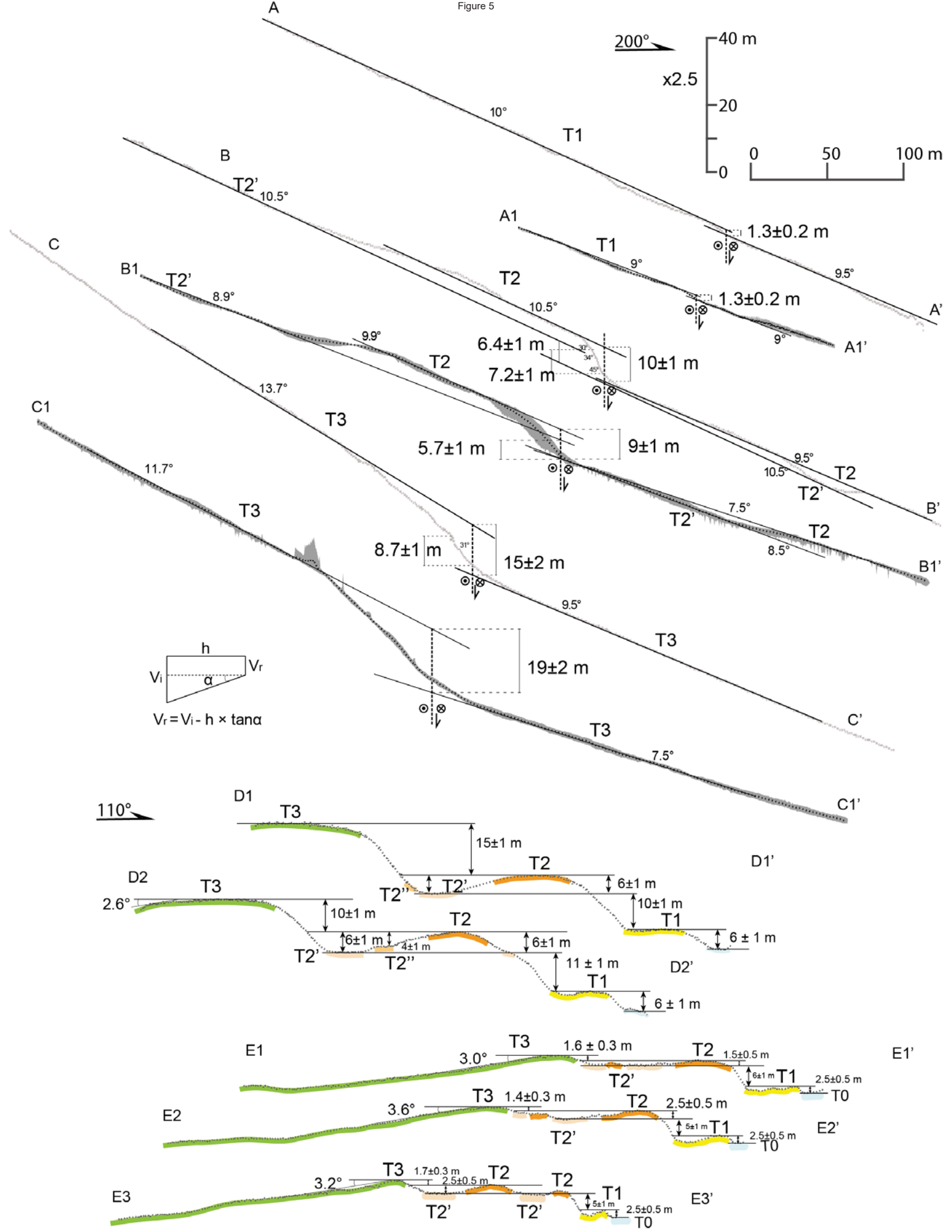
A
200°
40 m
x2.5
20
0
0
50
100 m
10°
T1
B
T2'
10.5°
A1
1.3±0.2 m
T1
9°
9.5°
A'
C
B1
T2'
8.9°
T2
10.5°
1.3±0.2 m
9°
A1'
9.9°
6.4±1 m
10±1 m
7.2±1 m
T2
13.7°
C1
T3
5.7±1 m
9±1 m
9.5°
10.5°
T2
T2'
B'
11.7°
T3
7.5°
T2'
T2
8.5°
B1'
8.7±1 m
15±2 m
9.5°
T3
h
Vi
Vr
α
19±2 m
Vr = Vi - h × tanα
C'
T3
7.5°
C1'
110°
D1
T3
15±1 m
T2
D1'
D2
T3
T2''
T2'
6±1 m
2.6°
10±1 m
10±1 m
T1
T2
6 ± 1 m
6±1 m
4±1 m
6±1 m
T2'
T2''
11 ± 1 m
D2'
T1
6 ± 1 m
E1
T3
1.6 ± 0.3 m
T2
1.5±0.5 m
E1'
3.0°
T2'
6±1 m
T1
2.5±0.5 m
T0
E2
T3
1.4±0.3 m
T2
2.5±0.5 m
3.6°
5±1 m
T1
E2'
T2'
2.5±0.5 m
T0
E3
T3
1.7±0.3 m
T2
T2
3.2°
2.5±0.5 m
T1
E3'
5±1 m
T2'
T2'
2.5±0.5 m
T0

Figure 6

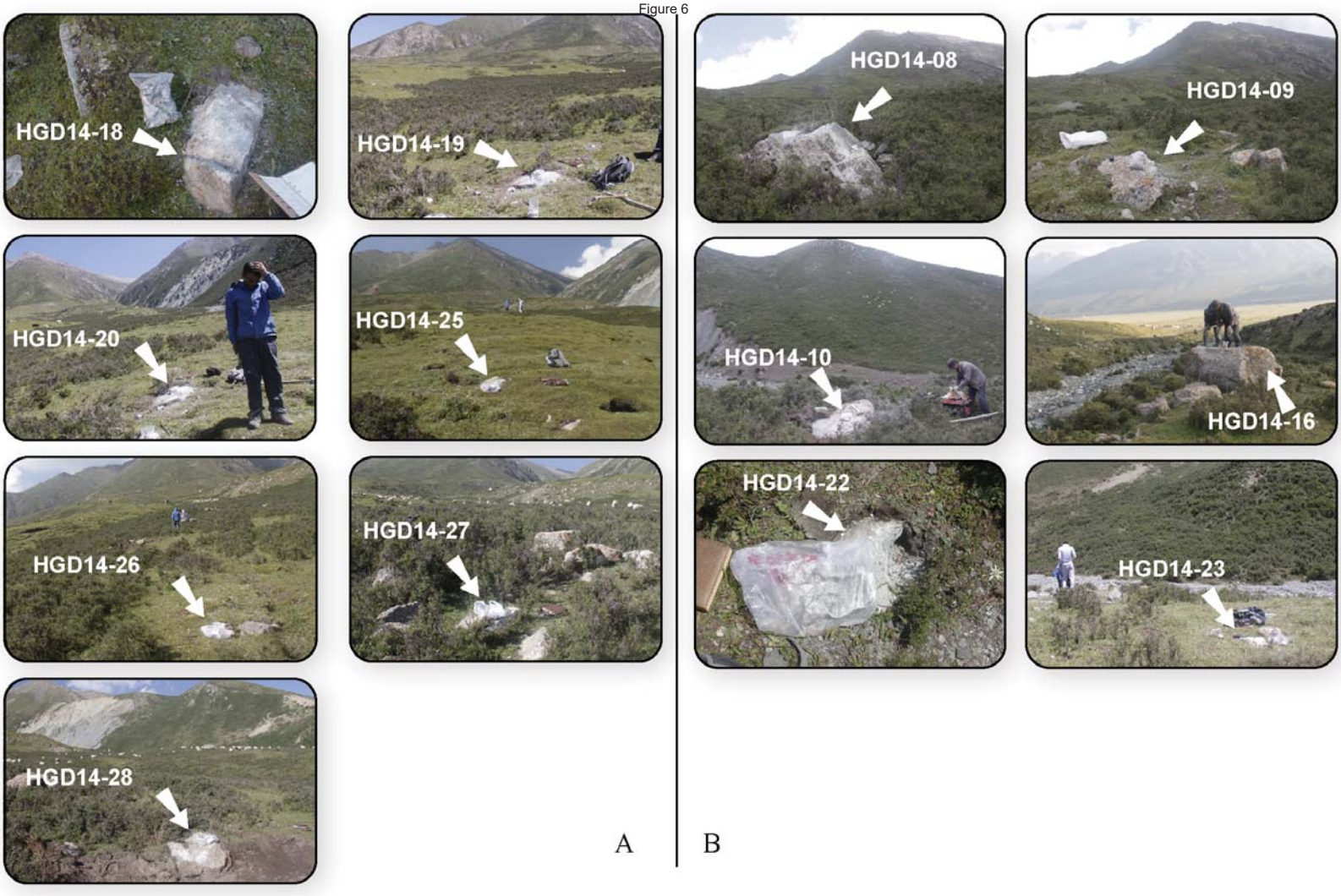
HGD14-18
HGD14-19
HGD14-08
HGD14-09
HGD14-20
HGD14-25
HGD14-10
HGD14-16
HGD14-26
HGD14-27
HGD14-22
HGD14-23
HGD14-28
A
B

Figure 7


A
~80cm

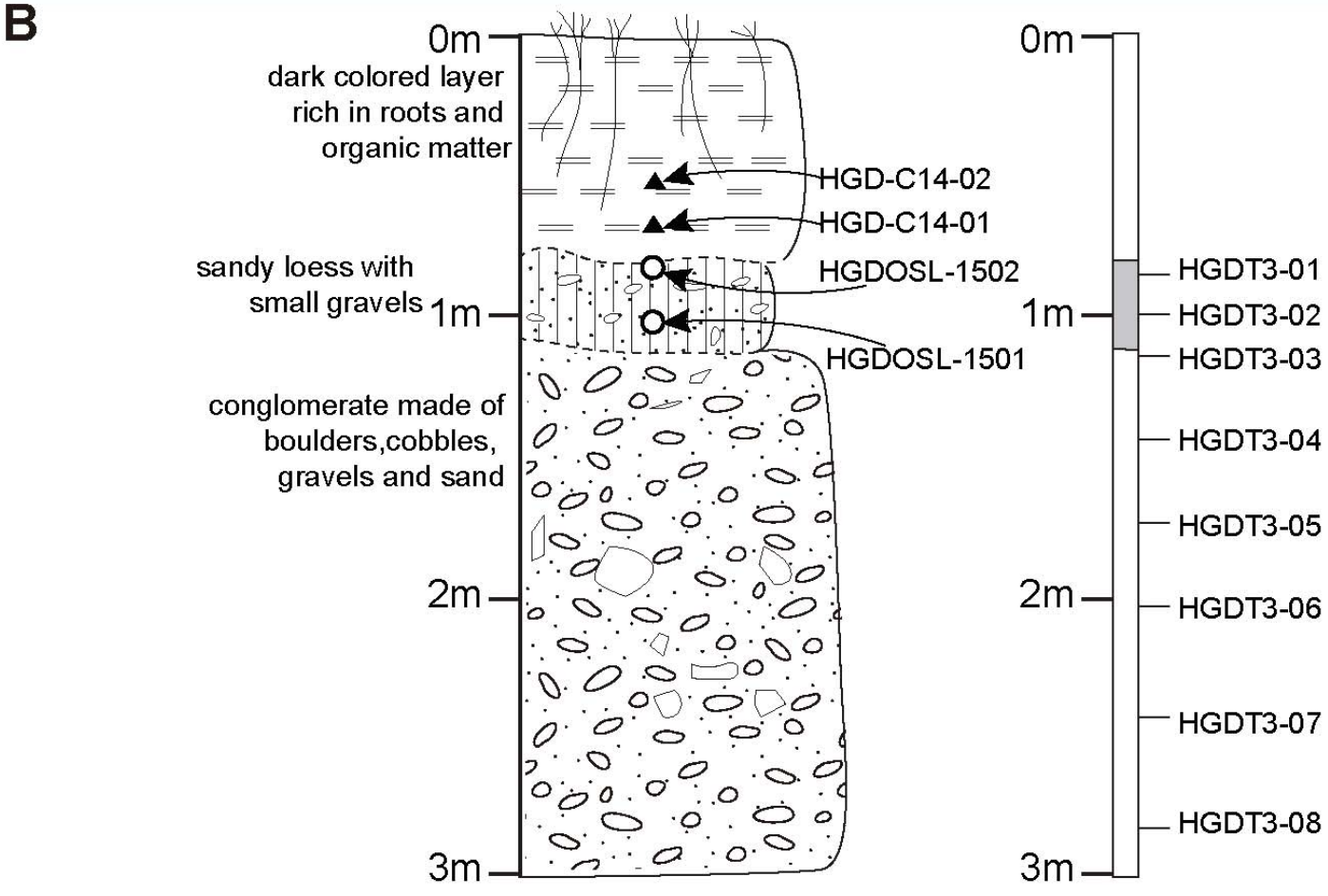
B
0m
dark colored layer
rich in roots and
organic matter
HGD-C14-02
HGD-C14-01
sandy loess with
small gravels
1m
HGDOSL-1502
HGDOSL-1501
conglomerate made of
boulders,cobbles,
gravels and sand
2m
3m
0m
1m
2m
3m
HGDT3-01
HGDT3-02
HGDT3-03
HGDT3-04
HGDT3-05
HGDT3-06
HGDT3-07
HGDT3-08

Figure 8

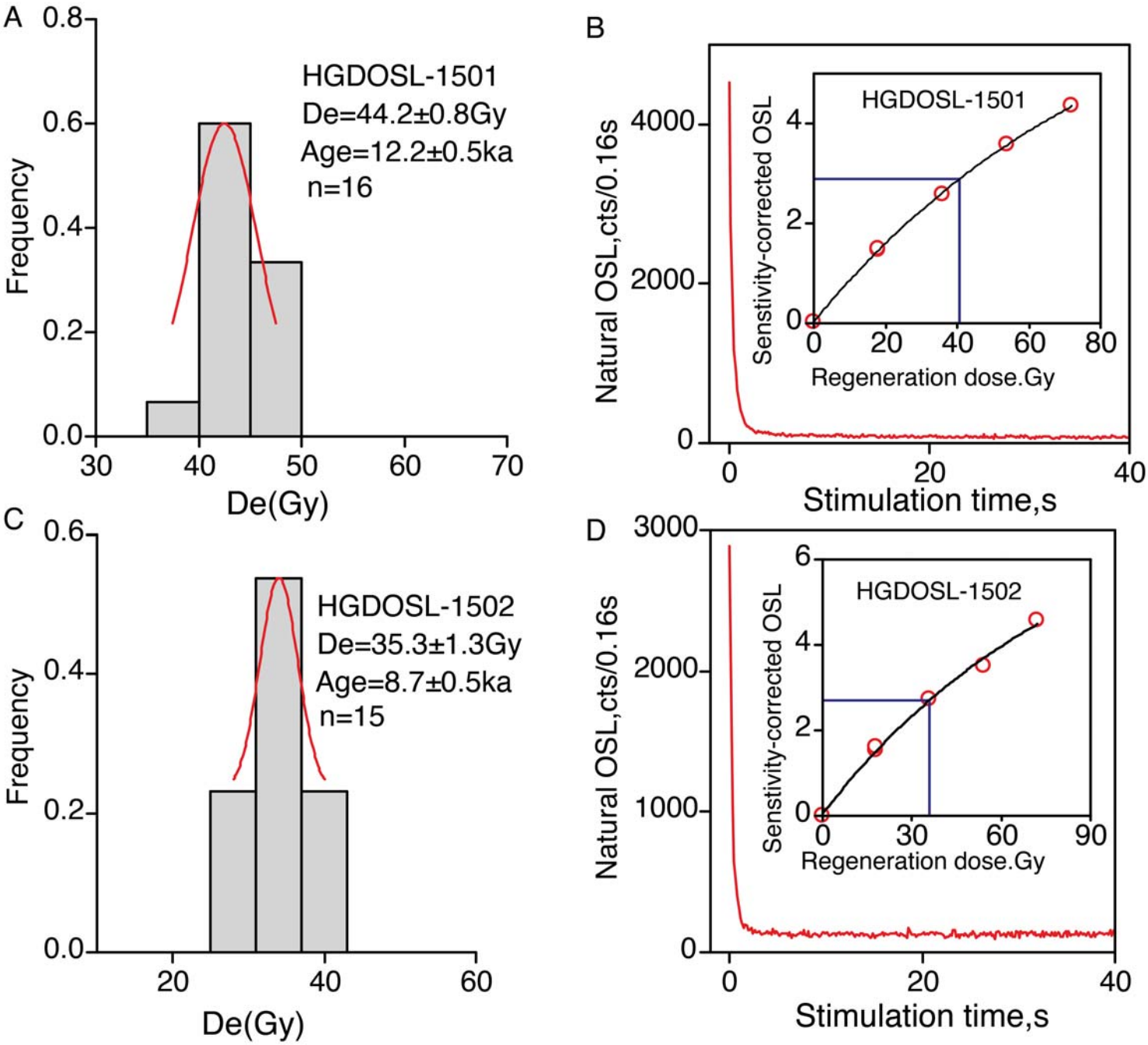
A
HGDOSL-1501
De=44.2±0.8Gy
Age=12.2±0.5ka
n=16
Frequency
De(Gy)
B
HGDOSL-1501
Natural OSL,cts/0.16s
Senstivity-corrected OSL
Regeneration dose.Gy
Stimulation time,s
C
HGDOSL-1502
De=35.3±1.3Gy
Age=8.7±0.5ka
n=15
Frequency
De(Gy)
D
HGDOSL-1502
Natural OSL,cts/0.16s
Senstivity-corrected OSL
Regeneration dose.Gy
Stimulation time,s

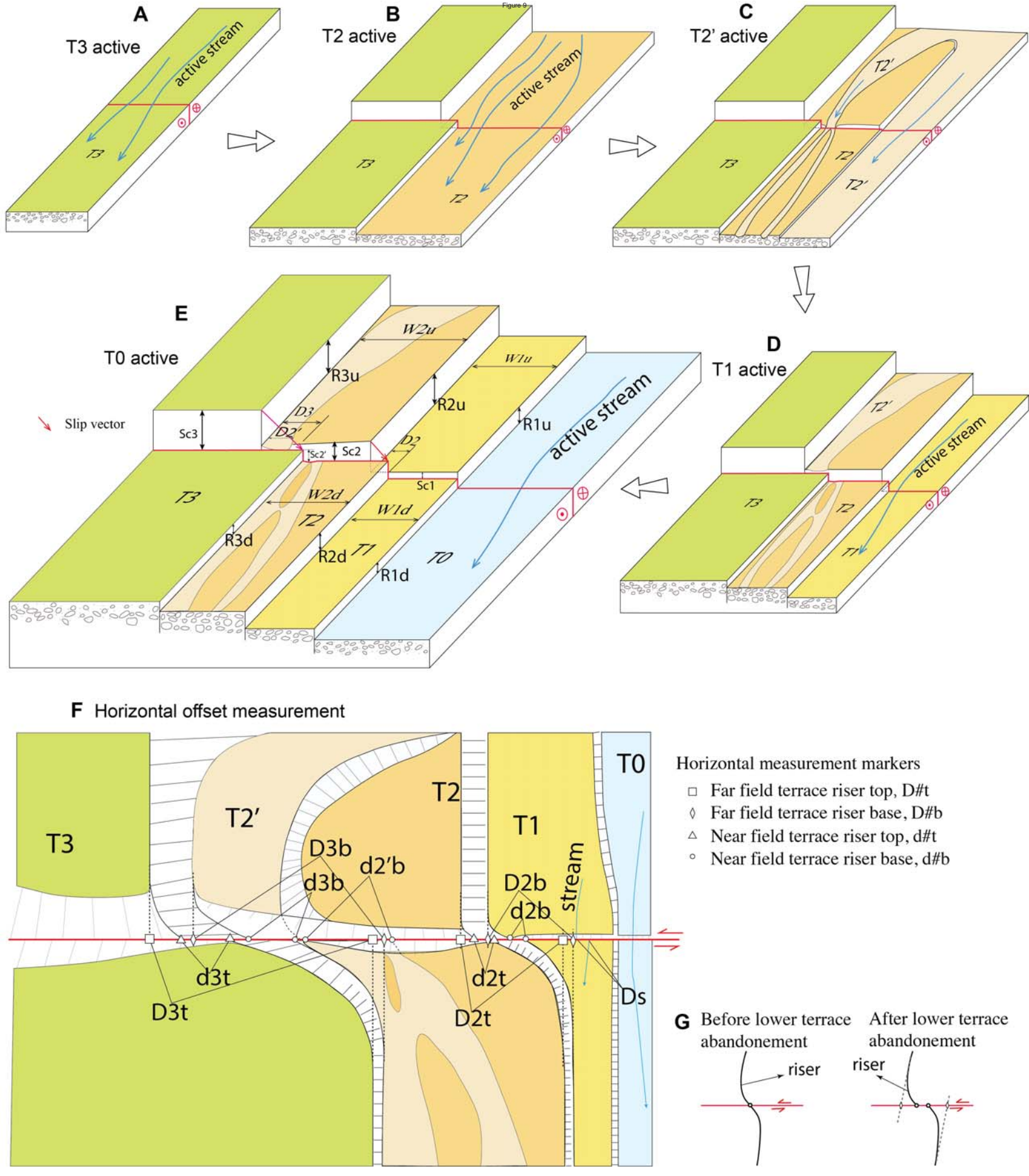
A
T3 active
active stream
T3
B
T2 active
active stream
T3
T2
C
T2' active
T2'
T3
T2
T2'
D
T1 active
T2'
active stream
T3
T2
T1
E
T0 active
W2u
W1u
R3u
R2u
R1u
active stream
Slip vector
Sc3
D3
D2'
Sc2'
Sc2
D2
Sc1
T3
W2d
W1d
T2
R3d
R2d
T1
R1d
T0

F Horizontal offset measurement
T3
T2'
T2
T1
T0
D3b
d3b
d2'b
D2b
d2b
stream
d3t
D3t
d2t
D2t
Ds
Horizontal measurement markers
□ Far field terrace riser top, D#t
◊ Far field terrace riser base, D#b
△ Near field terrace riser top, d#t
○ Near field terrace riser base, d#b
G Before lower terrace abandonement
riser
After lower terrace abandonement
riser

Figure 10

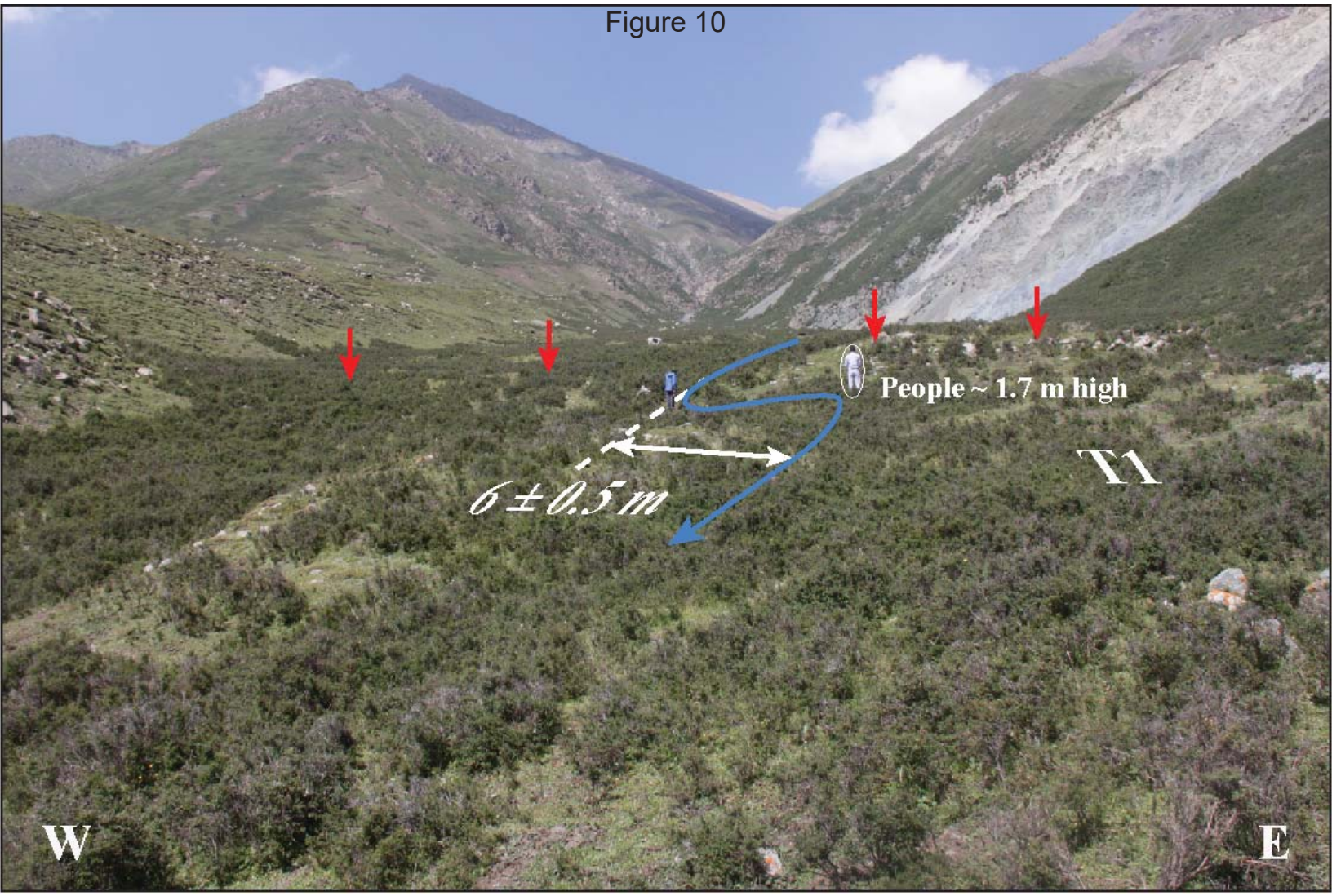

Figure 11

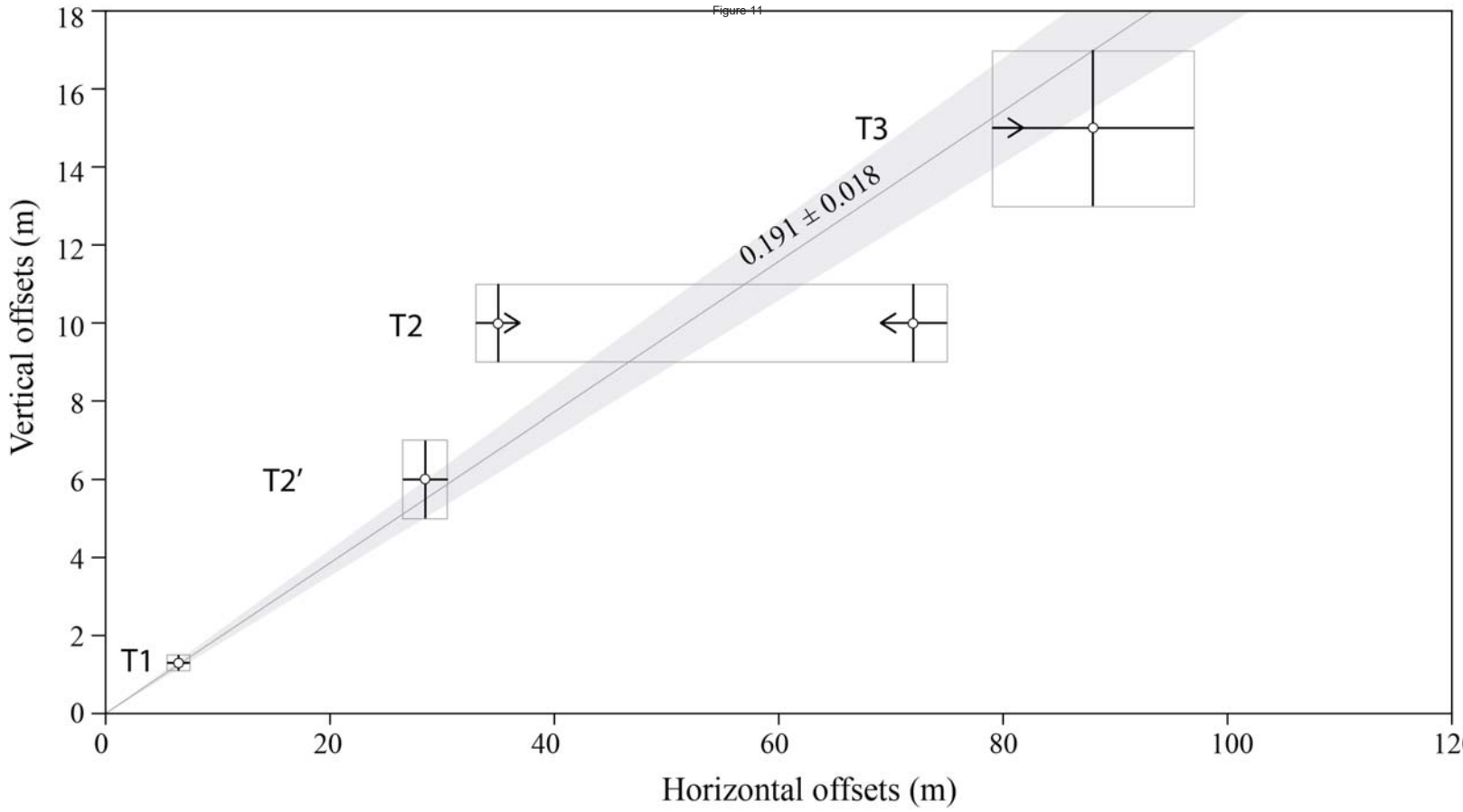
Vertical offsets (m)
Horizontal offsets (m)
0
2
4
6
8
10
12
14
16
18
0
20
40
60
80
100
120
T1
T2′
T2
T3
0.191 ± 0.018

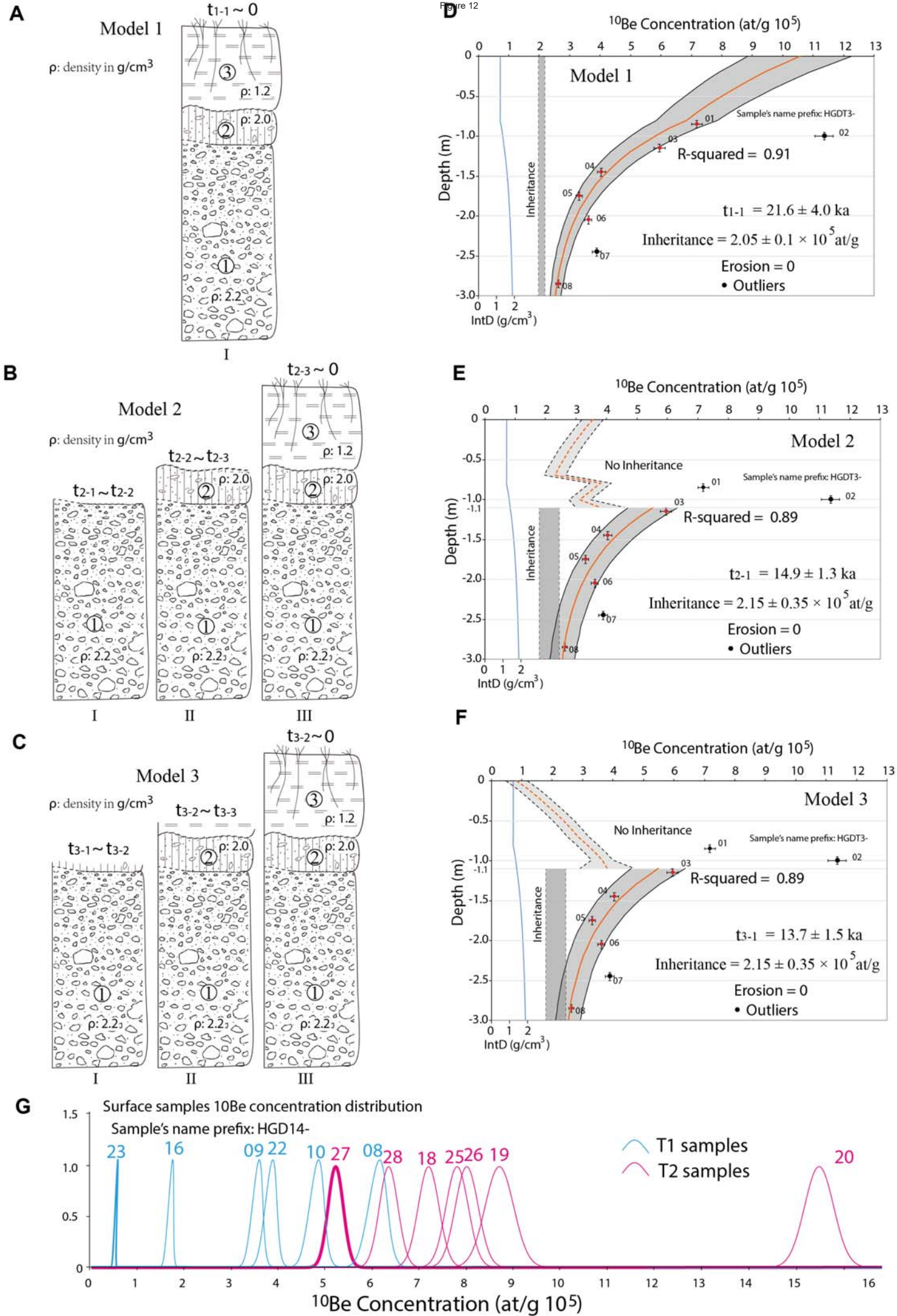
A
Model 1
ρ: density in g/cm3
t1-1 ~ 0
③
ρ: 1.2
②
ρ: 2.0
①
ρ: 2.2
I
B
Model 2
ρ: density in g/cm3
t2-3 ~ 0
t2-2 ~ t2-3
t2-1 ~ t2-2
ρ: 1.2
ρ: 2.0
ρ: 2.2
I
II
III
C
Model 3
ρ: density in g/cm3
t3-2 ~ 0
t3-2 ~ t3-3
t3-1 ~ t3-2
ρ: 1.2
ρ: 2.0
ρ: 2.2
I
II
III
D
10Be Concentration (at/g 10^5)
Model 1
Sample's name prefix: HGDT3-
R-squared = 0.91
t1-1 = 21.6 ± 4.0 ka
Inheritance = 2.05 ± 0.1 × 10^5 at/g
Erosion = 0
• Outliers
Depth (m)
Inheritance
IntD (g/cm3)
E
10Be Concentration (at/g 10^5)
Model 2
No Inheritance
Sample's name prefix: HGDT3-
R-squared = 0.89
t2-1 = 14.9 ± 1.3 ka
Inheritance = 2.15 ± 0.35 × 10^5 at/g
Erosion = 0
• Outliers
Depth (m)
Inheritance
IntD (g/cm3)
F
10Be Concentration (at/g 10^5)
Model 3
No Inheritance
Sample's name prefix: HGDT3-
R-squared = 0.89
t3-1 = 13.7 ± 1.5 ka
Inheritance = 2.15 ± 0.35 × 10^5 at/g
Erosion = 0
• Outliers
Depth (m)
Inheritance
IntD (g/cm3)
G
Surface samples 10Be concentration distribution
Sample's name prefix: HGD14-
23
16
09
22
10
27
08
28
18
25
26
19
20
T1 samples
T2 samples
10Be Concentration (at/g 10^5)

Figure 13

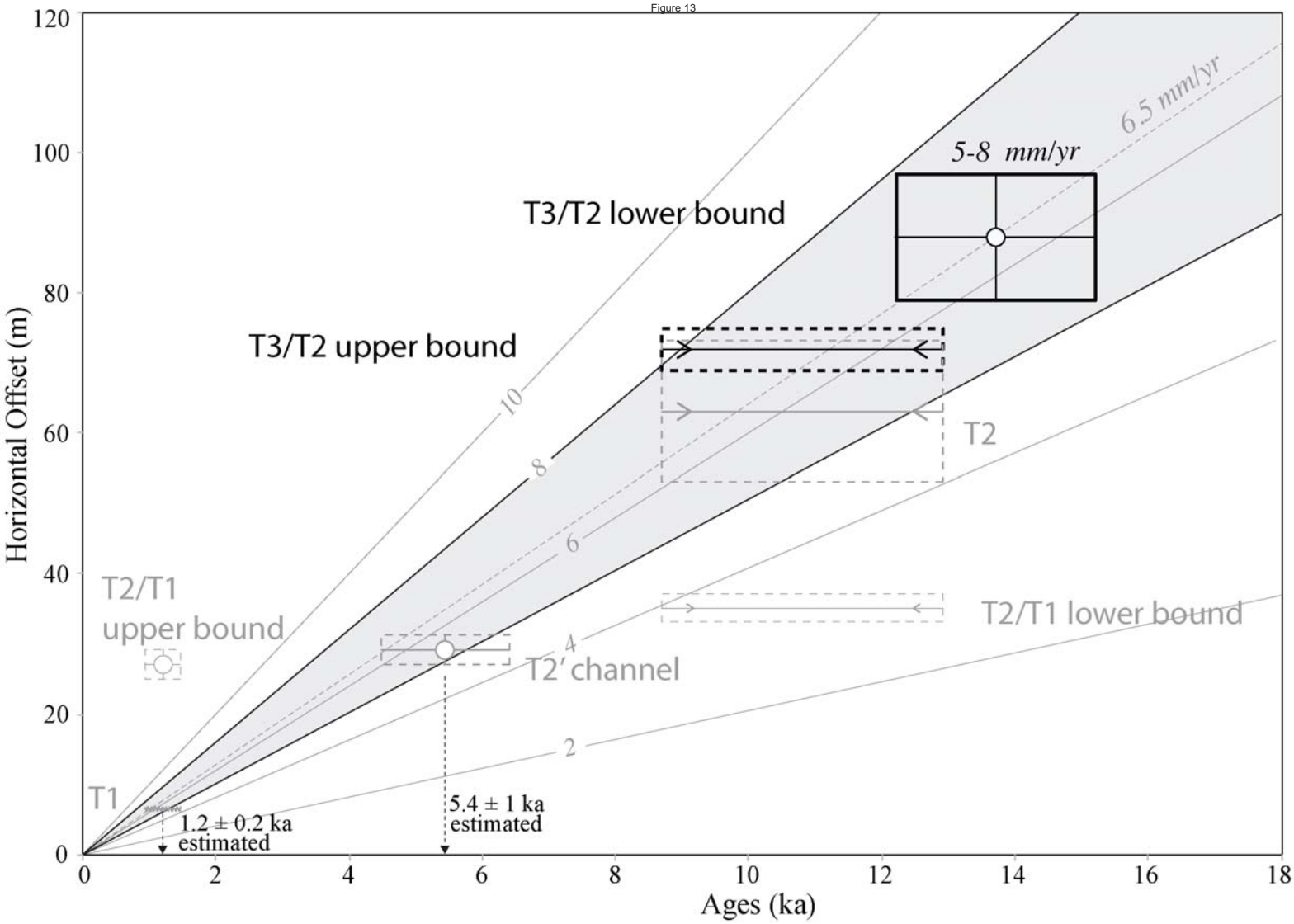
Horizontal Offset (m)
Ages (ka)
0
20
40
60
80
100
120
0
2
4
6
8
10
12
14
16
18
5-8 mm/yr
6.5 mm/yr
T3/T2 lower bound
T3/T2 upper bound
T2
T2/T1
upper bound
T2/T1 lower bound
T2′ channel
T1
1.2 ± 0.2 ka
estimated
5.4 ± 1 ka
estimated
10
8
6
4
2